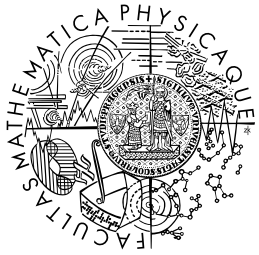

FACULTY
OF MATHEMATICS
AND PHYSICS
Charles University

BACHELOR THESIS

Sára Belejová

Microstructure and properties of Al-Li based alloys

Department of Physics of Materials

Supervisor of the bachelor thesis: doc. RNDr. Miroslav Cieslar, CSc.
Study programme: Physics
Study branch: General Physics

Prague 2021

I declare that I carried out this bachelor thesis independently, and only with the cited sources, literature and other professional sources. It has not been used to obtain another or the same degree.

I understand that my work relates to the rights and obligations under the Act No. 121/2000 Sb., the Copyright Act, as amended, in particular the fact that the Charles University has the right to conclude a license agreement on the use of this work as a school work pursuant to Section 60 subsection 1 of the Copyright Act.

In Prague date 24.5.2021 Sára Belejová

Author's signature

First of all, I would like to thank the supervisor of my work, doc. RNDr. Miroslav Cieslar for the acquaintance with the issue, help with all measurements, and a patience in adjusting this thesis to the final form. I also thank Mgr. Michal Hájek, Ph.D. for his help with resistometric measurements.

At the same time, I want to thank my consultant Mgr. Rostislav Králik and comrade-in-arms Bc. Lucia Bajtošová for answering and solving all problems with which I did not want to bother the supervisor.

Last but not least, thanks to my family, my boyfriend Jakub, and all the friends who supported me during my entire bachelor's degree.

Title: Microstructure and properties of Al-Li based alloys

Author: Sára Belejová

Department: Department of Physics of Materials

Supervisor: doc. RNDr. Miroslav Cieslar, CSc., Department of Physics of Materials

Abstract: This bachelor thesis is devoted to a study of rapidly solidified metallic strips prepared from two Al-Li-based alloys of the third generation. The aim of the thesis is to provide initial information about this new class of materials that could find application in aerospace industry. Al-Li third-generation alloys differ from previous generations by a lower Li content and thus by a type of main reinforcing phases. However, since conventional processings have already exhausted their possibilities that would significantly improve mechanical properties of these alloys, less traditional methods are tested, including rapid solidification processing by a melt-spinning method. These materials can achieve exceptional properties after milling and compactization thanks to finer microstructure and higher supersaturation of the solid solution. LOM, TEM (STEM) observations, and EDX analyses were used for the examination of the microstructure. In-situ resistometric measurements and in-situ TEM heating were performed to investigate the phase transitions. The structure of the alloys changes during heating. Grains of both alloys do not contain large particles after annealing. Only newly-formed coarse particles were observed on grain boundaries. The added scandium and zirconium resulted in a formation of a fine dispersion of reinforcing particles.

Keywords: Al-Li, microstructure, electron microscopy, rapid solidification

Názov bakalárskej práce: Mikroštruktúra a vlastnosti zliatin na báze Al-Li

Autor: Sára Belejová

Katedra: Katedra fyziky materiálov

Vedúci bakalárskej práce: doc. RNDr. Miroslav Cieslar, CSc., Katedra fyziky materiálov

Abstrakt: Táto bakalárska práca je venovaná štúdiu rýchlo utuhnutých kovových pásikov pripravených z dvoch zliatin na báze Al-Li tretej generácie. Cieľom práce je poskytnúť počiatočné informácie o tejto novej triede materiálov, ktoré by mohli nájsť uplatnenie v leteckom priemysle. Zliatiny Al-Li tretej generácie sa líšia od predchádzajúcich generácií nižším obsahom Li, a teda typom hlavných spevňovacích fáz. V dôsledku toho, že konvenčné procesy už vyčerpali svoje možnosti, ktoré by výrazne zlepšili mechanické vlastnosti týchto zliatin, testujú sa menej tradičné spôsoby vrátane procesu rýchleho tuhnutia tzv. melt-spinning metódou. Tieto materiály môžu dosiahnuť vynikajúce vlastnosti po rozomletí a kompaktizácií vďaka jemnejšej mikroštruktúre a vyššiemu presýteniu tuhého roztoku. Na skúmanie mikroštruktúry sa použili LOM, TEM (STEM) pozorovania a EDX analýzy. Pre skúmanie fázových prechodov boli uskutočnené rezistometrické in-situ merania a in-situ zahrievanie v TEM. Štruktúra zliatin sa počas zahrievania zmenila. Vnútro zŕn oboch zliatin neobsahuje po žíhaní veľké častice. Na hraniciach zŕn boli pozorované iba novovzniknuté hrubé častice. Pridané skandium a zirkónium viedli k tvorbe malých spevňujúcich častíc.

Kľúčové slová: Al-Li, mikroštruktúra, elektrónová mikroskopia, rýchle tuhnutie

Contents

Introduction **2**

1 Theoretical introduction **3**
1.1 Binary phase diagrams . . . 3
1.1.1 Thermodynamic derivation . . . 3
1.1.2 Eutectic and peritectic binary phase diagrams . . . 5
1.2 Al-Li-Cu-Mg-Zr-Sc alloys . . . 6
1.3 Rapid solidification . . . 7
1.3.1 Melt-spinning . . . 8

2 Experimental methods **9**
2.1 Materials . . . 9
2.2 Transmission electron microscopy . . . 9
2.2.1 Sample preparation for STEM observation . . . 10
2.2.2 Energy-dispersive X-ray spectroscopy . . . 12
2.2.3 Electron diffraction . . . 13
2.3 Resistometry . . . 13
2.3.1 Sample preparation for resistivity measurements . . . 14
2.4 Light optical microscopy (LOM) . . . 14

3 Results **15**
3.1 Light optical microscopy observations . . . 15
3.2 Initial state - STEM and EDX analysis . . . 16
3.3 Resistivity measurement . . . 19
3.4 STEM observation of in-situ heating . . . 22
3.4.1 AlLi alloy . . . 22
3.4.2 AlLiSc alloy . . . 23
3.5 Final state . . . 27

4 Discussion **32**

Conclusion **35**

Bibliography **36**

List of Figures **38**

List of Tables **40**

List of Abbreviations **41**

Introduction

Since the day of the first engine-driven flight, aircraft designers have been looking for lightweight materials. The strength/weight ratio (specific strength) is still a prime driver for materials selection of major importance. Aluminum proved to be the most suitable candidate for aircraft manufacture since it is lightweight and strong. Moreover, its high resistance to corrosion ensures the safety of the aircraft and its passengers.

Throughout the years (especially in the period between the First and the Second World Wars), with the development of the aviation and the space industry, there were increasing demands on the materials used, leading to the development and use of many different aluminum alloys. In the early years, aluminum alloys were developed by trial and error, but advancing understanding of the relationships among composition, processing, microstructural characteristics, and properties led to improvements important to aircraft applications. This bachelor thesis is focused on Al-Li based alloys. This class of alloys significantly reduces the weight of the aircraft and thus increases a fuel efficiency. However, their formability, ductility, fracture toughness and an anisotropy of mechanical properties are still an issue to be solved. The current generation of available Al–Li products is the third generation. This generation of Al-Li alloys partially mitigates some of negative features while retaining a reduction in material density.

A further improvement of mechanical properties of these alloys consists in an adjusting of the chemical composition. Added elements could form new strengthening phases or influence the degree of recrystallization. Once the possibilities for the improvement in this way have been exhausted, new technological procedures should be used for a further progress in their development. Rapid solidification methods are offered as options for this improvement. Rapid heat extraction leads to the formation of new non-equilibrium phases and to a finer (in some cases even amorphous) structure.

In this work, we have focused on the investigation of the microstructure of Al-Li-Cu-Mg-Zr and Al-Li-Cu-Mg-Zr-Sc alloys, which were prepared by rapid solidification processing by a melt-spinning method. This material is not yet conventionally produced but may have exceptional properties after milling and compactization. The first chapter of the thesis is focused on the recognition of phase diagrams and main phases in alloys containing the above-mentioned alloying elements, and also the melt-spinning method is introduced. In the second chapter, the basic research methods used in the experimental part of this work, such as electron microscopy and resistometric measurements are described. The third chapter includes the results of measurements and observations. Last two chapters contain a discussion of results, and a summary of main outcomes.

1. Theoretical introduction

1.1 Binary phase diagrams

Phase diagrams show material phases in equilibrium under certain external conditions, such as temperature or pressure. Well-recognized phases are solid, liquid or gaseous phases. However, a definition of a phase as a state of matter with uniform physical properties gives a new wide range of possible solid phases that differ by their crystal structure, e.g., graphite and diamond.

In physical metallurgy, phase diagrams could describe processes such as melting, solidification, dissolution and precipitation or phase transitions in studied materials. Understanding phase transitions can help to optimize materials, e.g., by a proper heat treatment to obtain better properties (usually strength, hardness, stiffness or ductility). Phase diagrams used in physical metallurgy differ from classic pressure-temperature phase diagrams. As the object of the study is not a pure substance but a system composed of two or more chemical substances, there is a necessity to work with a new variable - the composition. Therefore, in order to describe for example a two-component system, binary phase diagrams are used.

1.1.1 Thermodynamic derivation

In thermodynamics, an equilibrium state is obtained by minimizing the thermodynamic potentials. In an isolated system where temperature and volume remain constant, the minimum of Helmholtz free energy $F = E - TS$ is used to describe the equilibrium state. E is the internal energy, T is the temperature, and S is the entropy of the system. Considering a binary system where the interaction between the substances is permitted, molar free energy F can be expressed as:

$$F = n_A F_A + n_B F_B + F^M, \tag{1.1}$$

where n_A, n_B are molar fractions of A and B components, F_A, F_B are molar free energies of pure substances A and B, and F^M is a mixing term ($F^M = E^M - TS^M$).

Using statistical thermodynamics of ideal solutions the entropy of mixing can be derived:

$$S^M = -Nk(\nu_A ln\nu_A + \nu_B ln\nu_B). \tag{1.2}$$

To include an interaction of atoms, it is necessary to consider the model of regular solutions, where atoms are surrounded by atoms of the same or different species with some probability and where the entropy of mixing of ideal solution can be used. After a short derivation (showed in [1]) we have:

$$F^M = Nn\nu_A\nu_B\varepsilon + NkT(\nu_A ln\nu_A + \nu_B ln\nu_B). \tag{1.3}$$

Where N is the number of atoms in the system, n is the number of 'neighbors' of an atom, k is Boltzman constant, T is the temperature of the system, and ε is the so-called exchange energy. It is given by an expression $\varepsilon = \varepsilon_{AB} - \frac{1}{2}(\varepsilon_{AA} + \varepsilon_{BB})$, where ε_{AA} is an energy of interaction between two A atoms, ε_{AB} is an energy of interaction between an A and a B atom etc.

When $\varepsilon < 0$, the system is preferably composed of AB bonds. On the contrary, the system is preferably composed of the AA or BB bonds when the exchange energy is greater than 0 (for $\varepsilon = 0$, the solution is ideal).

Once an expression for free energy has been found it can be plotted as a function of a composition at a given temperature (Fig. 1.1).

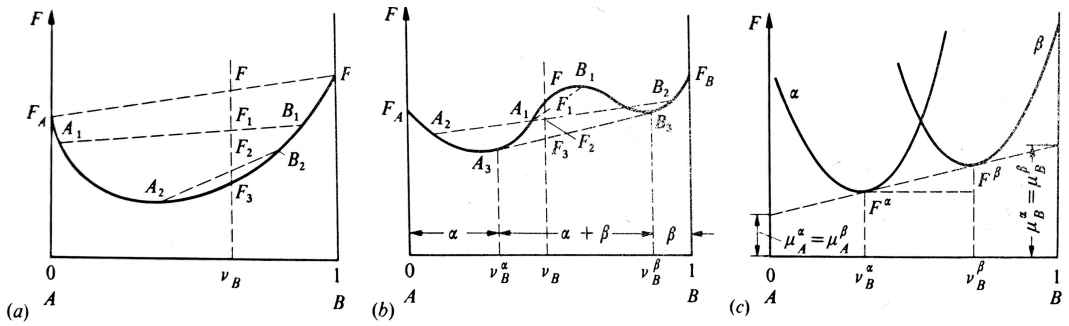

Fig. 1.1: Free energy and common tangent construction [1].

For the low exchange energy ε and high temperatures, the second term in Eq. 1.3 predominates, and the result is a parabola open at the top (see Fig. 1.1a). With increasing ε, the shape of the F curve changes, and in some areas, it is more favorable for the system to separate into two phases α and β where the final free energy is lower. This is demonstrated in Fig. 1.1b and Fig. 1.1c and because the final energy lays on the common tangent of the F curve at points A_3 and B_3 this construction is called *the common tangent construction* and corresponds to the equilibrium condition for phases α and β given by equality of chemical potential ($\mu_A^\alpha = \mu_A^\beta$ and $\mu_B^\alpha = \mu_B^\beta$).

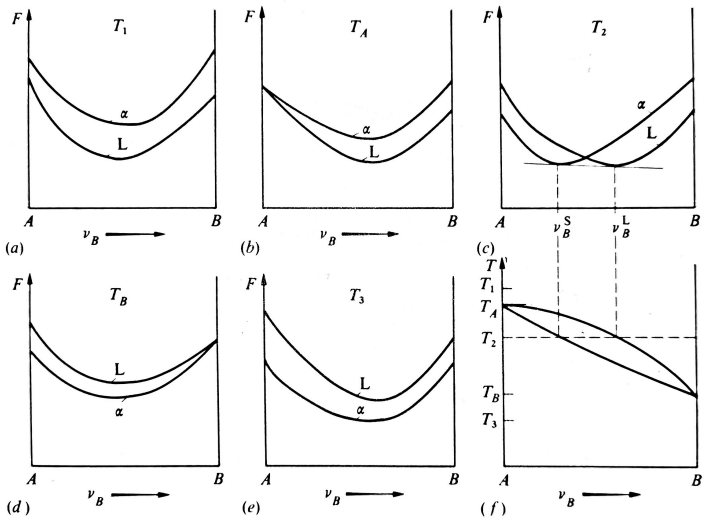

Fig. 1.2: Derivation of a binary phase diagram from free energy curves for solid phase α and melt phase L [1].

Assuming an alloy or a system entirely miscible in the liquid and solid states, the free energy of both states is parabola, which depends on temperature (see Fig. 1.2a to e). The system will exist in the state with a lower free energy

(Fig. 1.2f): for temperature T_1 the system will remain liquid regardless of the composition, for temperature T_3 the system will remain solid and for the temperature $T \in (T_A, T_B)$ the system will be found in different phases depending on its composition (solid, liquid or $L + \alpha$ phase with the compositions ν_B^α and ν_B^β).

1.1.2 Eutectic and peritectic binary phase diagrams

When solid states of components A and B are not entirely miscible in each other, the free energy curve for the solid-state is different, as shown in Fig. 1.3. A phase diagram with two different solid phases α_1, α_2 and their coexistence with the liquid phase and each other appears as a result. This type of phase diagram is called the eutectic binary phase diagram and it is characterized with an eutectic point at the eutectic temperature T_E (T_4 at Fig. 1.3), at which all the melt solidifies.

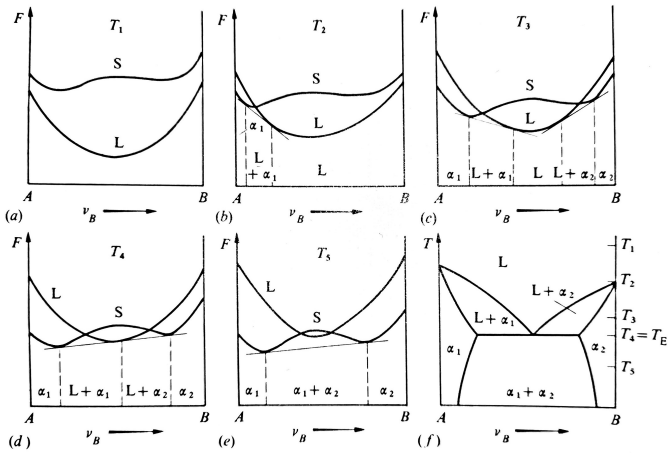

Fig. 1.3: Derivation of an eutectic binary phase diagram from free energy evolution at different temperatures [1].

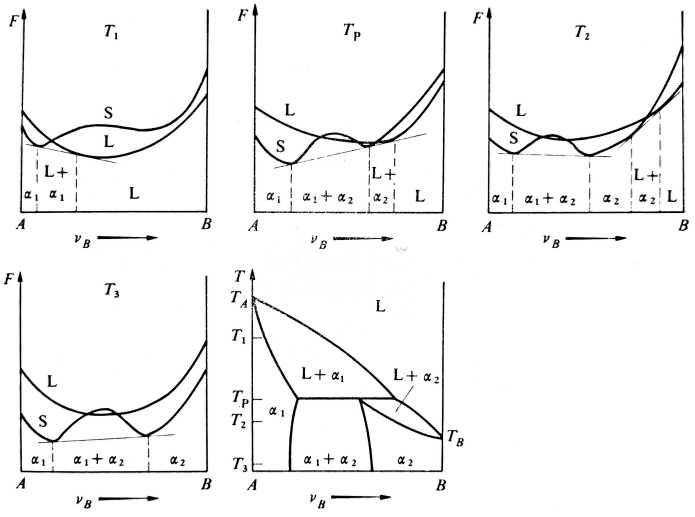

Fig. 1.4: Derivation of peritectic binary phase diagram from free energy evolution at different temperatures [1].

Another type of the binary phase diagram is called peritectic. The formation of this diagram is also derived from the free energy of a liquid and a solid-state of A and B components and it is shown in Fig. 1.4. The diagram is characterized by a peritectic point at peritectic temperature T_P. This type of diagram is observed in compounds with a large difference in their melting points.

As the majority of commercially used alloys consist of more than two components, it is logical that the above mentioned binary phase diagrams serve just as a simplification. Their use is valid for the binary systems with negligible admixtures. When the admixture is no longer negligible, ternary and other multi-component phase diagrams have to be used.

1.2 Al-Li-Cu-Mg-Zr-Sc alloys

Aluminum alloys and their development in general are typically associated with aircraft and aerospace industry. The first aluminum alloy in the aircraft industry was used during the Wright brothers' flight in 1903 [2]. It was an Al-Cu alloy (9 wt.% Cu) with a specific yield strength of 43 MPa/g/cm^3 used in the crankcase of the engine. For a comparison, alloy 7055-T7751 - the strongest aluminum alloy used for upper wings nowadays, has the specific compressive strength of 229 MPa/g/cm^3 [3].

One of the significant steps towards a new success of Al-based alloys has been the addition of Li and a following development of Al-Li alloys of the first, second and the latest third generation. The first addition of Li to Al for the alloy properties improvement was reported in the middle of the 1920s. However, it took almost another 40 years for Al-Li-based alloy to be used in the aircraft industry. The main advantages of the lithium addition are a decrease in density (approximately 3% per 1 wt.% Li), and an increase in Young's elastic modulus (approximately 6% per 1 wt.% Li) [2]. These improvements are achieved mainly because of the Al_3Li (δ') phase that has a large intrinsic modulus. Strengthening of the alloy by Al_3Li phase is caused by the coherency and surface hardening, modulus hardening, and order hardening. In order to form other strengthening phases, elements such as Cu and Mg are added to Al-Li alloys.

Co-precipitation of Cu-based phases with Al_3Li forms extra strengthening phases such as Al_2CuLi (T_1) or Al_6CuLi_3 (T_2) - both of them shown in Fig. 1.5. The motion of dislocations through Al_2CuLi precipitates are energetically non-favorable, and hence they serve as effective barriers, increasing the strength of the material.

The addition of Mg to Al-Li alloys may result in a formation of a metastable S′ - Al_2CuMg (stable S phase is shown in Fig. 1.6) that forms near grain boundaries. The existence of these precipitates causes a reduction or even an elimination of precipitation-free zones (PFZ). PFZ are considered to be regions of weakness in the material, and their presence causes a decrease in the ductility of Al-Cu-Li alloys [4].

There are also some disadvantages in using Al-Li alloys. In general, the alloy formability, ductility, and fracture toughness could decrease. Also, an anisotropy of mechanical properties is often observed. Some of the effects might be suppressed by a grain size reduction, recrystallization degree controlling, or by an addition of other alloying elements.

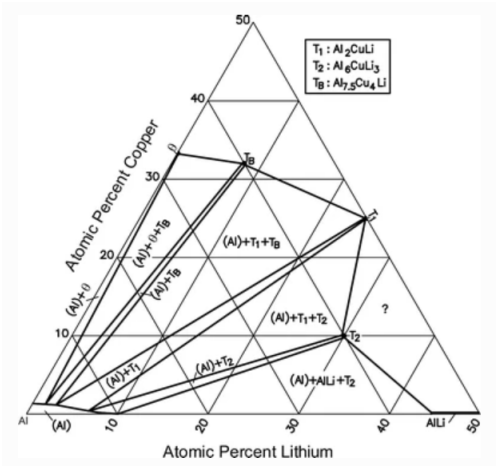

Fig. 1.5: Al-rich region of the computed Al-Cu-Li ternary phase diagram at 500°C [5].

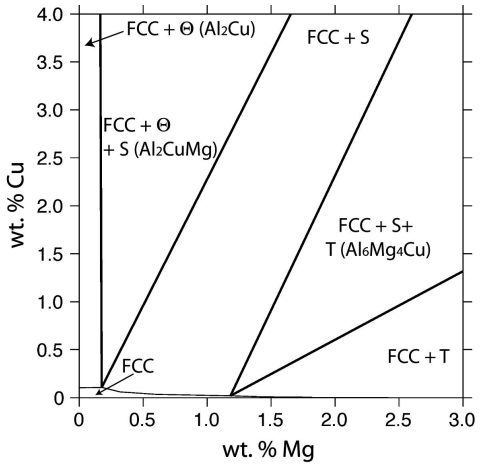

Fig. 1.6: Al-rich corner of the Al-Cu-Mg ternary phase diagram at 200°C [6].

Interesting combinations of properties after adding scandium and zirconium have been found [7]. The metastable phases of $Al_3Sc_{1-x}Zr_x$ (Fig. 1.7), which precipitate during aging, contribute to the increase of the strength of the alloy by precipitation hardening in this case. However, these phases transform into coarse equilibrium phases at high temperatures when they lose the original strengthening effect.

The common phase in aluminum alloys containing Cu as a reinforcing element and Fe as an impurity is Al_7Cu_2Fe [8]. These are intermetallic particles with deteriorating effects on the alloy properties.

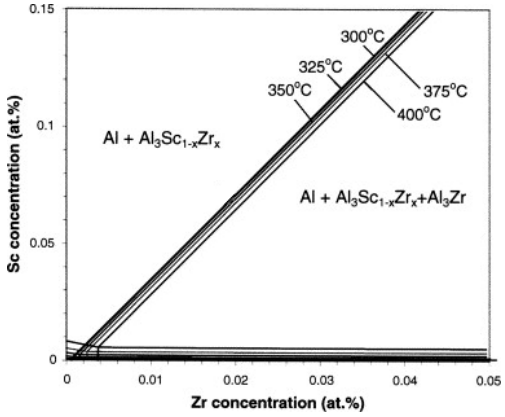

Fig. 1.7: Al-rich corner of isothermal section of the computed Al-Sc-Zr ternary phase diagram [9].

1.3 Rapid solidification

Rapid solidification processing is an alloy preparation method growing in popularity nowadays. It improves grain refinement and the chemical homogeneity of the alloys which cannot be achieved by a conventional alloy casting. The cooling rate of this process should be greater than 10^3K/s. The cooling rate means a tangent

of a cooling curve - a curve in a temperature-over-time diagram representing the change of phase of the matter.

The main principle used to achieve rapid solidification is to fragment the molten material into droplets (atomization) or to cast a melt on a cooled substrate to form continuous products most often ribbons (melt-spinning).

1.3.1 Melt-spinning

The melt-spinning technique is often used to obtain amorphous metal or metallic glassy alloys as the cooling rate reaches 10^6 Ks^{-1}. The product of this process is in a form of thin ribbons. The approach was introduced by Pol Duwez et al. in 1960 [10] and helped to invent many binary, ternary, and multicomponent amorphous materials ever since.

Generally, small pieces of an alloy (5-100g) are placed inside a container heated by an induction coil. The container is usually made of quartz glass or a boron nitride as it must resist high temperatures. After applying high current to the coils, the content of the container melts. The molten metallic drops are subsequently ejected by an argon-pressurization onto a fast-rotating wheel through a thin nozzle. The wheel is usually made of copper, rotates at 5000-7000 rpm [11] and is being cooled from inside. The principle of the method is schematically shown in Fig. 1.8, resulting ribbons in Fig. 1.9.

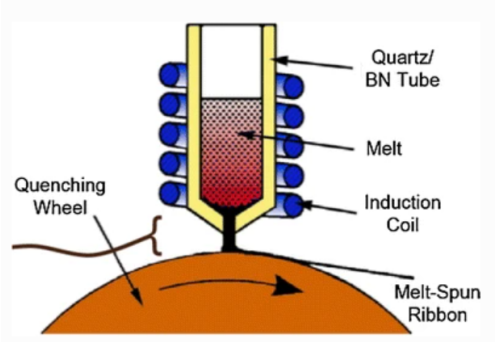

Fig. 1.8: Schematics of the melt-spinning process (the RSP used in the thesis for the sample preparation) [12].

Fig. 1.9: An example of an alloy prepared by melt-spinning.

2. Experimental methods

2.1 Materials

The studied materials were prepared in the Institute of Physics SAS in Bratislava from master alloys marked as V242 and V243 by melt-spinning method. The compositions of master alloys are shown in Table 2.1 and Table 2.2. The main difference is in the presence of Sc in the V243 alloy.

Tabuľka 2.1: Chemical composition of the master aluminum alloy V242

Element	**Al**	**Cu**	**Li**	**Mg**	**Zr**	**Sc**	**Ag**	**Fe**	**Other**
Content, wt.%	95.99	2.52	0.72	0.27	0.12	-	0.33	0.09	Balance

Tabuľka 2.2: Chemical composition of the master aluminum alloy V243

Element	**Al**	**Cu**	**Li**	**Mg**	**Zr**	**Sc**	**Ag**	**Fe**	**Other**
Content, wt.%	95.32	2.61	0.71	0.27	0.10	0.17	0.29	0.09	Balance

Boron-nitride (BN) nozzle, measuring 6 x 0.8 mm^2, was used in the process. The alloys were heated to 1000 °C. The cooled cylinder with a diameter of 470 mm was in a distance of 0.22 mm from the nozzle at a speed of 1500 rpm. The nozzle firing pressure was close to 320 mbar.

For a clear orientation in the text, we will refer to the material prepared from the V242 pre-alloy as AlLi and the material prepared from the V243 pre-alloy as AlLiSc.

2.2 Transmission electron microscopy

Transmission electron microscope (TEM) is one of the most powerful tools in biology and material science laboratories. In contrast to the light optical microscope (LOM), it uses an electron beam instead of light source and electromagnetic lenses instead of glass lenses. Thanks to its high resolution, it can be used for observations of structures such as submicroscopic cell structures, macromolecules, and viruses.

In material science, TEM is usually used for observations of microstructure (and defects) up to the atomic level, crystal structure determination, and chemical analyses.

The limitation of the resolution of the light optical microscope was explained by Ernst Abbe in the 1870s [13]. The principle says that the microscope can not produce an image of an object smaller than the length of the wave produced by the illumination source. In LOM, the illumination source is a visible light of the given range of wavelengths from about 380 to 750 nm. This principle limits the resolution of LOM to approximately 0.2 μm, while the current limiting resolution of TEM is about 0.05 nm [14].

Despite the discovery of an electron by J.J. Thomson in 1897 [15], the wave nature of electrons was not understood until the publication of a De Broglie hypothesis in 1924 [16]. Thanks to the first electromagnetic lens design in 1891, transmission electron microscopy was invented in 1931-1934 by M. Knoll and E. Rusko at the Technical University of Berlin [17,18].

Ordinary transmission electron microscope (see Fig. 2.1) consists of an electron gun that produces accelerated electrons, followed by electromagnetic condenser lenses. They are used to condense the electron beam and adjust the size of the electron beam transmitting the specimen. The specimen is placed between pole pieces of the objective lens in a special holder.

Due to the interaction of the electron beam with the specimen, transmitted, diffracted, backscattered, and secondary electrons are produced. The last two types of electrons are generally used to obtain an image in the scanning electron microscopy (SEM), and the first two types create an image in the transmission electron microscopy.

The objective lens is used to form a diffraction pattern in the back focal plane of the TEM, and therefore both, diffraction pattern and image are simultaneously present in TEM.

Objective aperture, placed in the back focal plane, is used in imaging mode for the selection of one or more beams that contribute to the final image. Based on which beam contribute to the resulting image, we denote the obtained image by the abbreviation BF (bright field), DF (dark field) or HRTEM (high resolution TEM).

The intermediate lens placed between the objective lens and the projector lens is used for changing the focusing position either on a diffraction pattern (diffraction mode) or a TEM image (imaging mode), as shown in Fig. 2.1. Switching from the real space (image) to the reciprocal space (diffraction pattern) is therefore achieved by the change of the strength of this lens.

The projector lens is used to magnify the image that appears in the second intermediate image plane, and that is finally projected at a fluorescent screen or recorded by CCD (Charged Coupled Device) camera.

Much work in this bachelor thesis has been done using STEM mode of the transmission electron microscope. The principle difference is in specimen irradiation (see Fig. 2.2). While a conventional TEM image is generated by illuminating through the whole specimen area, in the STEM mode, a raster illumination is made. The electron beam is focused to a fine spot that is scanned over the sample. Special focus on individual points of the specimen makes this operating mode suitable for several analytical techniques, from which we will introduce energy-dispersive X-ray spectroscopy in more detail. STEM image guaranteed by a bright field detector is similar to BF image in conventional TEM, while upper dark field (UDF) detector registers the Z-contrast (the intensity is higher in points containing atoms with higher atomic number - Z).

2.2.1 Sample preparation for STEM observation

A small piece of the original ribbon has been manually polished on SiC grinding papers (on the surface, which has not been in contact with the cooling cylinder during melt-spinning) to the thickness of approximately 0.1 mm.

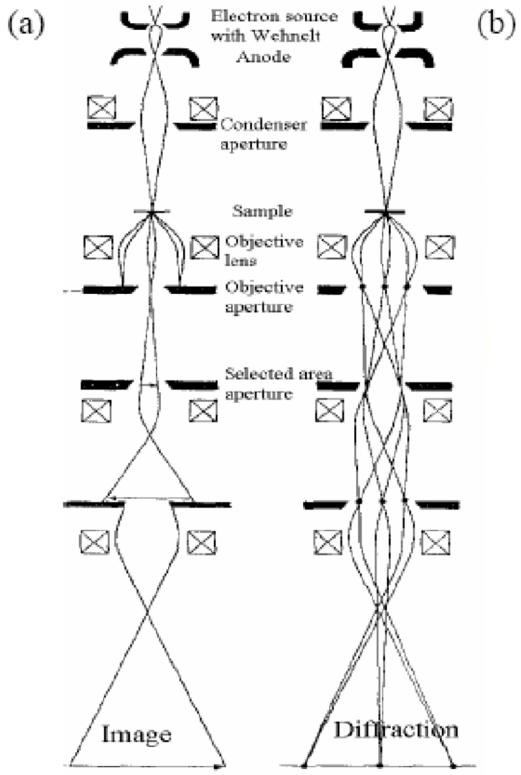

Fig. 2.1: Imaging (a) and diffraction (b) mode of the transmission electron microscope [19].

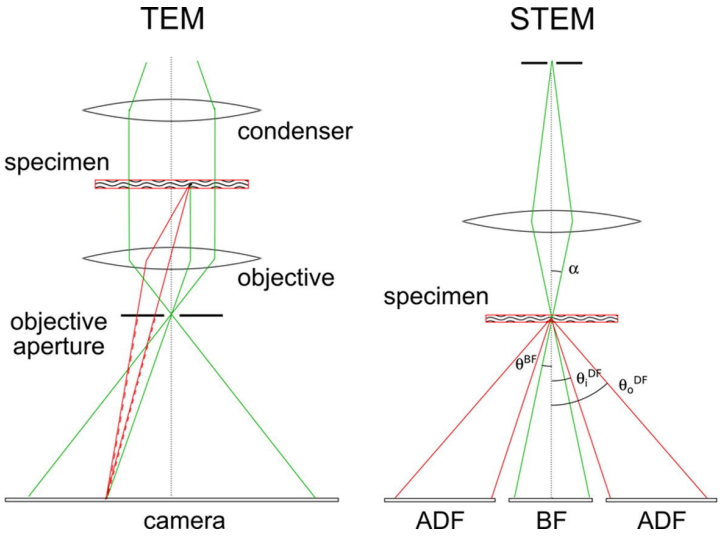

Fig. 2.2: Conventional and scanning transmission electron microscope scheme comparison [20]. Electron beam is focused to one point in STEM mode while in conventional TEM mode electrons fall perpendicular to a large area of the sample surface.

Circular discs of diameter 3 mm were mechanically punched out of the thinned aluminum ribbon. Subsequently, the discs were electrolytically etched by 30 vol.% HNO_3 acid in methanol at the temperature -20 °C and a voltage of 16.5 V. After about one minute, a small hole (ideally in the middle of the disc) was formed, surrounded by an area of an extremely thin material suitable for the STEM/TEM observation. The electrolytic etching was done using the device TenuPol − 5.

Transmission electron microscopy was performed on a JEOL JEM 2000FX microscope at an accelerating voltage of 200 kV.

2.2.2 Energy-dispersive X-ray spectroscopy

Energy-dispersive X-ray spectroscopy is an analytical technique used for chemical analysis of the chosen area of the sample.

The technique is known under abbreviations EDX, EDS, EDXS, XEDS. However, it can be referenced under energy dispersive X-ray analysis (EDXA) or even energy dispersive X-ray microanalysis (EDXMA).

In the process, the sample is being bombarded by high-energy electrons, as a result of which, electrons from the inner shells of the atom are being ejected. The created empty place in the inner shell must be fastly refilled with the electron from the higher energy atomic level. During this transition, the electron is losing part of its energy by emitting the characteristic X-rays that are being detected. As the name of emitted rays suggests, the energy released during the process is unique to each element in the periodic table, which is the key to the chemical analysis of the sample.

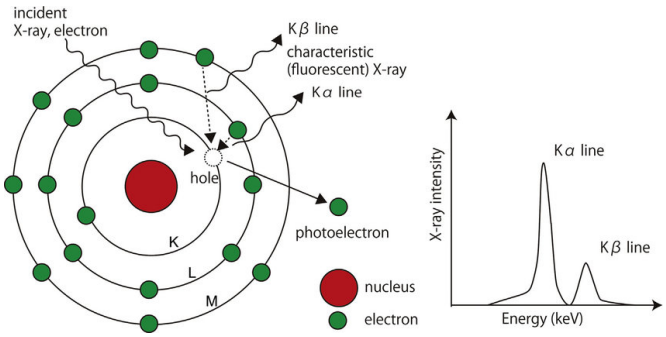

Fig. 2.3: Scheme for characteristic X-ray notation [21].

With more than one energy level of atoms, there comes some more terminology, schematically explained at Fig. 2.3. First of all, we distinguish whether the vacancy has been generated at the first (K), second (L), third (M), or further energy level (counting from the nucleus). Secondly, we add the greek letter α, β, γ, etc., according to the difference between skipped energy levels. For example, when the electron came from the L energy level to the K energy level of aluminum notation is AlKα.

A typical result of EDX is a graph with keV on the x-axis and peak intensity on the y-axis.

In physical metallurgy, EDX, together with diffraction patterns observation, helps to determine the phases of observed particles.

2.2.3 Electron diffraction

Using TEM in diffraction mode (see Fig. 2.1) reveals atomic arrangements of the studied material. As the electrons penetrate the specimen, they are being scattered. This process creates the diffraction pattern that reveals the arrangement of molecules and atoms in a crystalline specimen. By analyzing the distances of spots in the diffraction pattern, it is possible to determine the interplanar distance in the crystal lattice of the studied specimen area, and partially identify the phase present in the studied specimen.

2.3 Resistometry

Electrical resistometry is one of the most common methods for the study of alloys. Its essence is to monitor changes (decreases or increases) in the resistivity of the material.

Electrical resistivity or also called specific electrical resistance ρ is a property of the material that quantifies how strongly it resists or conducts electric current. The lower the resistivity is, the easier the material allows electric current pass through. It is the reciprocal of electrical conductivity σ standing in Ohm's law.

$$\vec{j} = \sigma \vec{E} = \frac{1}{\rho} \vec{E}. \tag{2.1}$$

The resistivity of a crystalline metallic specimen can be described by an empirical rule named after a british scientist Augustus Matthiessen, who studied the electrical conduction of metals and alloys in the middle of 19th century, Matthiessen's rule [22]:

$$\rho = \rho_{imp} + \rho_{latt}(T), \tag{2.2}$$

where $\rho_{latt}(T) \to 0$ as thermodynamic temperature $T \to 0$ and ρ_{imp} is independent of T.

The rule is based on the proportionality of electrical resistance to the scattering probability of conduction electrons. This probability arises with the temperature due to the vibrations of the crystal lattice. The resistivity ρ_{imp} is given by the irregularities of the crystal lattice since the wavefunction of the electron fits the regular lattice.

Suggesting a low concentration of irregularities the member ρ_{imp} can be rewritten as a sum of the resistivity contribution ρ_k from every impurity in the first approximation:

$$\rho_{imp} = \sum_k \rho_k = \sum_k \beta_k c_k, \tag{2.3}$$

where c_k expresses the concentration of the k-th type of the impurity and β_k is a proportionality constant that is in general independent of temperature.

Deviations from Matthiessen's rule during the process of metal annealing indicate a phase transformation and change of the microstructure of the alloy. These deviations can easily be observed as local extrema at derivation curve $\frac{1}{\rho_0}\frac{d\rho}{dT}$.

Resistometry measurement can be done as a measurement of residual resistance or as an in-situ measurement of the resistance.

In the first case the specimen is being annealed up to a desired temperature, quenched and subsequently immersed in liquid nitrogen where the resistance is measured. For the true value of residual resistance we would need to measure the resistivity at 0 K. For graphic representation, a relative resistivity curve $-\frac{\rho}{\rho_0}$ and a derivation curve $-\frac{1}{\rho_0}\frac{d\rho}{dT}$ are used.

The second case, in-situ measurement, is a direct measurement of resistance during linear heating of a specimen.

2.3.1 Sample preparation for resistivity measurements

Resistance was measured using a four-probe method with Keithley devices [23]. Samples of the length 15 cm were cut from the aluminum ribbon, subsequently cut at both ends (to secure the contacts), and folded in half with the mica in the middle to prevent mutual contact.

The sample thus prepared was placed into a furnace with a protective argon atmosphere that prevents oxidation at higher temperatures.

2.4 Light optical microscopy (LOM)

Light optical microscopy observations were performed at the beginning of the work to provide a basic overview of the structure of the material. Observations were performed on Zeiss Axio Observer 7 LOM.

For sample preparation, a piece of a strip was cut from the sample material and cast with a resin into a better handling cylindrical mold. Subsequently, samples were mechanically polished using SiC grinding papers. Then they were further polished using 3 μm and 1 μm diamond suspensions in water and finally using an OPS suspension.

In the end, samples were electrolytically etched using the material as an anode and HBO_4 in water solution as an electrolyte. This process is called Barker etch method and is employed to facilitate grain observations. The electrolyte used in the method is therefore also called Barker's reagent. A polished surface can be analyzed by a polarized light.

3. Results

3.1 Light optical microscopy observations

A basic overview of AlLi and AlLiSc sample microstructure is shown in Fig. 3.1 and Fig. 3.2. In Fig. 3.1a and Fig. 3.2a, the arrows indicate the direction in which the ribbon was solidified on the cylinder (RD - rolling direction) and the direction perpendicular to the rolling direction (ND - normal direction). All images in the LOM are taken from a view perpendicular to both the rolling and the normal direction (TD - transverse direction).

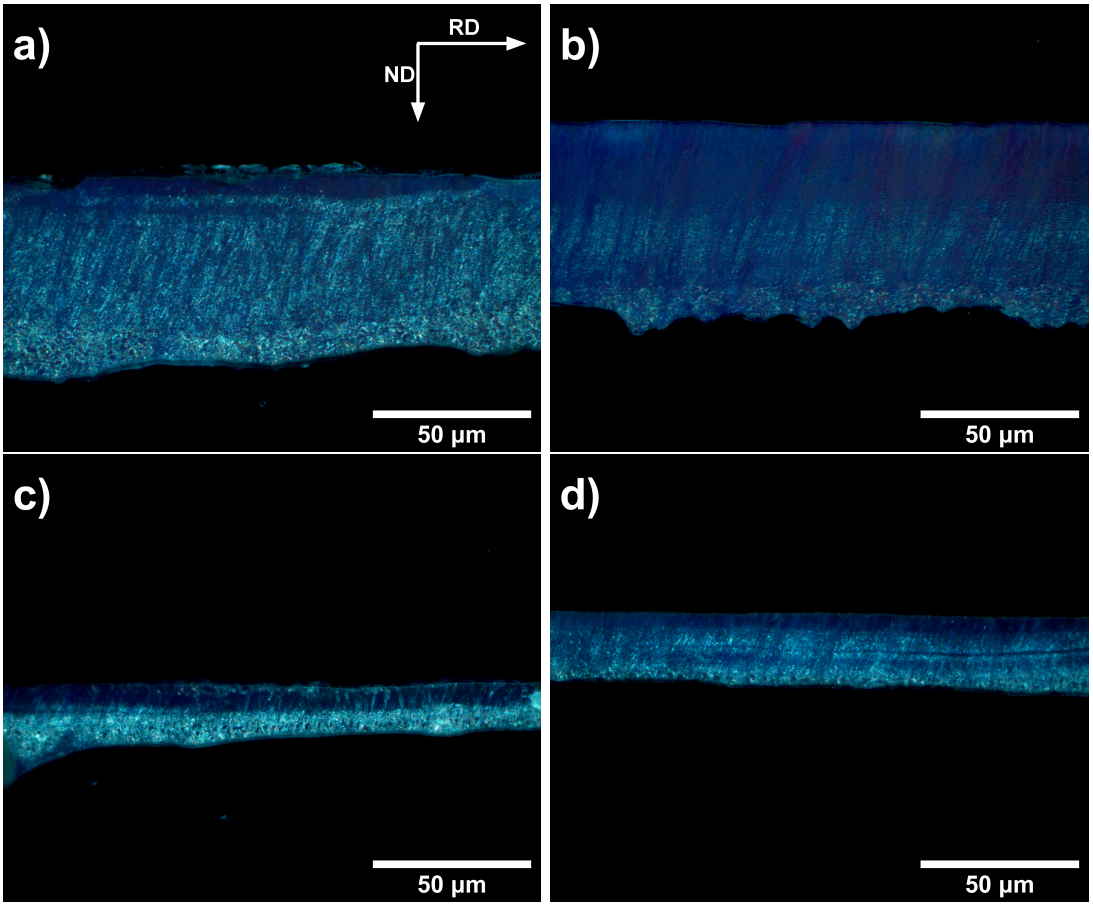

Fig. 3.1: Sections through the AlLi RSD ribbon.

The thickness of the ribbon is quite inhomogeneous. While in Fig. 3.1c the thickness of the ribbon is 14 µm, in Fig. 3.1a it is up to 66 µm. The surface, which has been in contact with the cooling cylinder during melt-spinning, is relatively smooth (upper part of ribbons in Fig. 3.1), but the surface on the opposite side is bumpy. The grain structure is fine to amorphous at the side where the material touched the cylinder during melt-spinning (or at least it is not distinguishable by LOM). However, with an increasing distance from the cylinder, microstructure changes, and discrete grains could be recognized. The width of the amorphous part is not the same throughout the sample (the grain size does not grow linearly with the distance from the cylinder surface; compare Fig. 3.1a and Fig. 3.1b. The

width of the amorphous part may be related to the adhesion of a given part of the ribbon to the surface of the rotating cylinder.

The thickness of the AlLiSc sample (see Fig. 3.2) is even more inhomogeneous and it can be noted that the sample is thicker than in the AlLi one. In Fig. 3.2b the thickness of the ribbon is about 50 μm while in Fig. 3.2d it is almost 120 μm.

The side of the AlLiSc sample where the material touched the cylinder during melt-spinning (upper part of ribbons in Fig. 3.2) has a much smoother surface. Overall, the grain structure is more homogeneous compared to the AlLi alloy but amorphous only in several places.

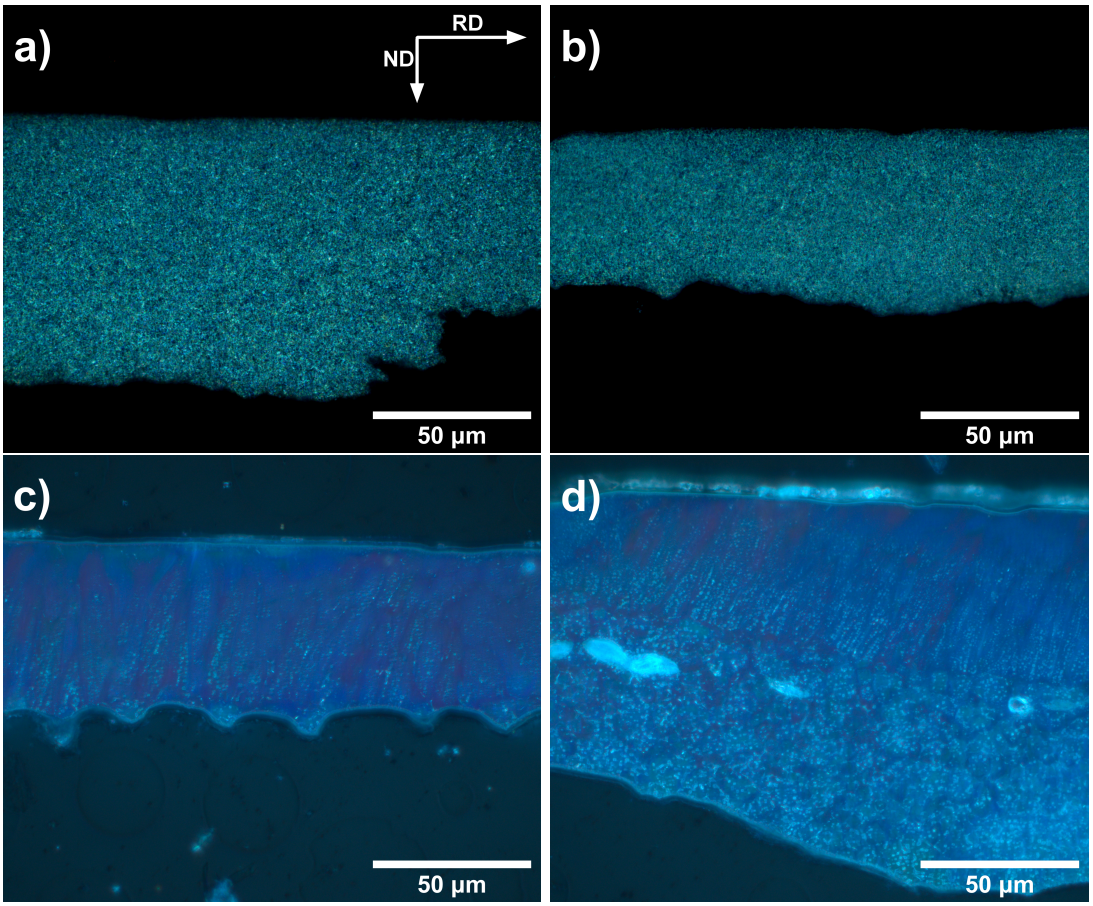

Fig. 3.2: Sections through the AlLiSc RSD ribbon.

3.2 Initial state - STEM and EDX analysis

As a part of STEM observations, we first made overview images of both alloys in the initial state at small magnifications. Although samples were polished at the side, which has not been in contact with the cooling cylinder, a clear crystal structure was always observed in both alloys. An example of the observed microstructure is shown in Fig. 3.3. It can be seen that the grain dimensions are in units of micrometers. However, as has already been evident from LOM, the grain size observed in the samples dramatically depends on distance from the surface. Fig. 3.3 also shows primary phase particles inside the grains and at the

grain boundaries. These primary phases are shown in more details in Fig. 3.4 and Fig. 3.5, which was taken at higher magnifications.

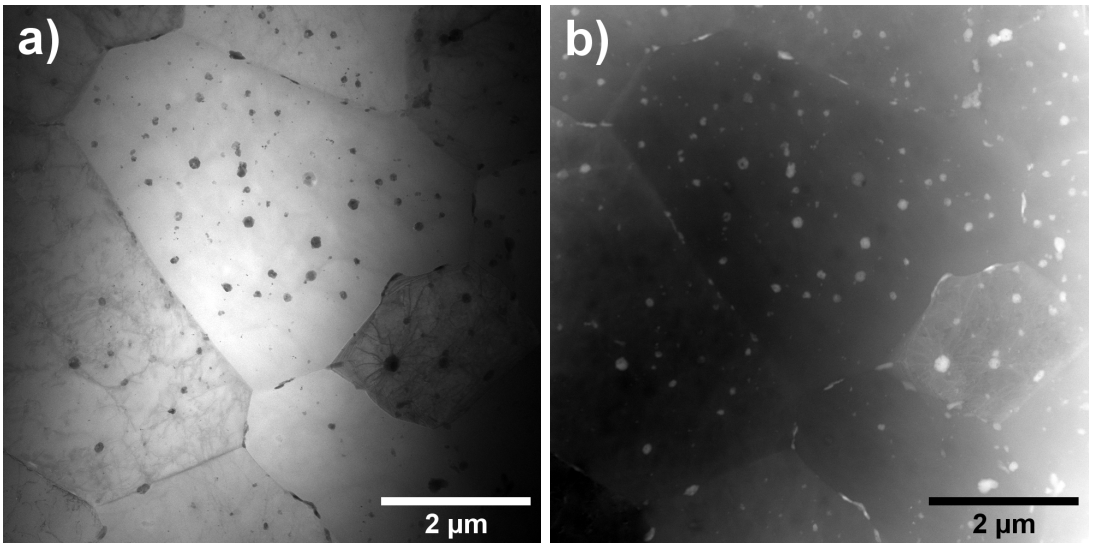

Fig. 3.3: STEM overview of the AlLiSc alloy in BF (a) and UDF (b) contrasts.

Fig. 3.4a shows spherical particles inside the grain of AlLi alloy (and residual dislocations), Fig. 3.4b shows detail at the grain boundaries.

Fig. 3.5a shows similar spherical particles inside grains of AlLiSc alloy, with a diameter of about 50 nm, and Fig. 3.5b shows a triple point between the grains.

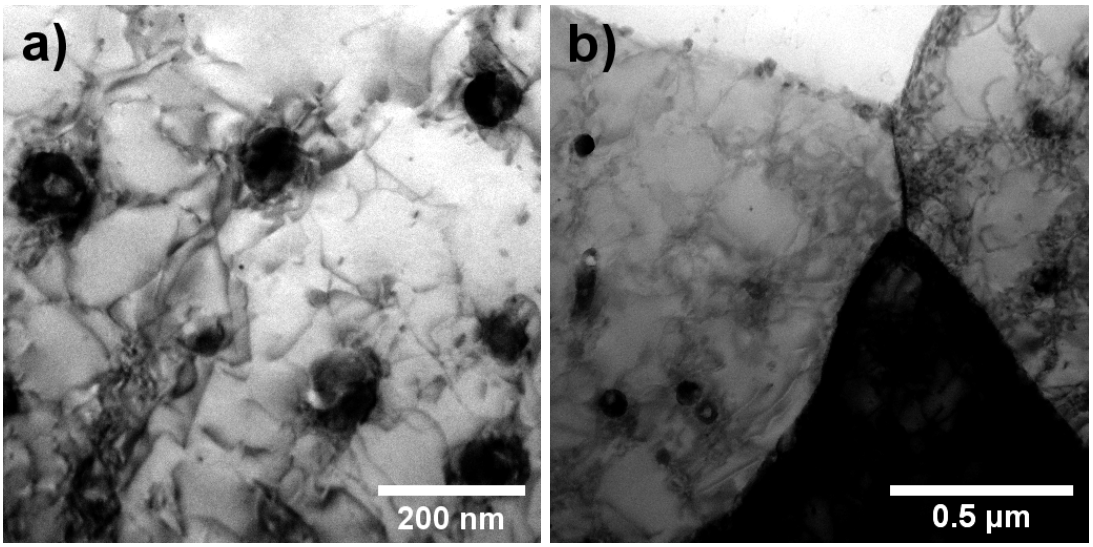

Fig. 3.4: Detailed TEM images of the AlLi alloy.

To determine the distribution of alloying elements in the studied alloys, we performed EDX mapping at multiple places on the AlLi and AlLiSc samples. The EDX maps were generated for: Al, Cu, Fe, Mg, Zr, Sc, and Ag (the lithium characteristic radiation is indistinguishable by EDX).

In the AlLiSc alloy, the distribution of additives Mg, Zr, Sc, and Ag was rather homogeneous over the entire sample for all EDX maps. The example of

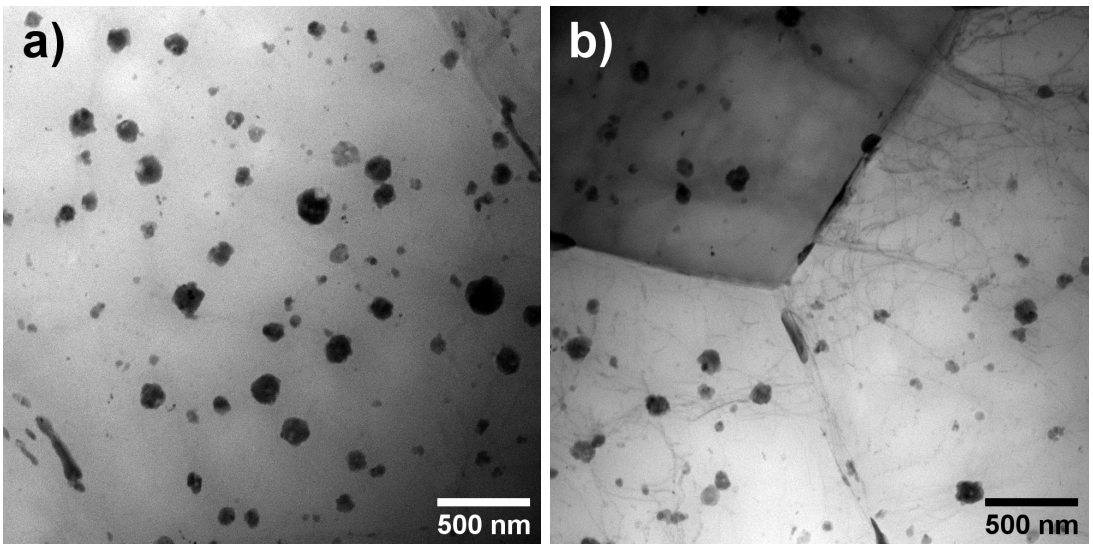

Fig. 3.5: STEM detailed images of the AlLiSc alloy.

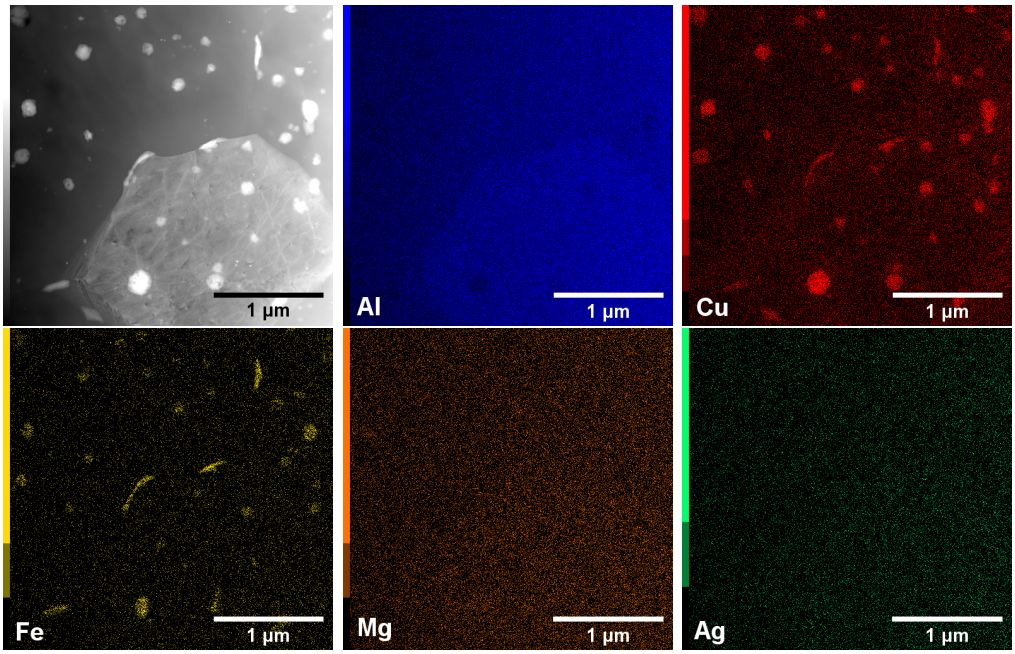

Fig. 3.6: STEM-UDF and EDX maps of the AlLiSc alloy (selected detail from Fig. 3.3).

the distribution of Al, Cu, Fe, Mg and Ag is shown in Fig. 3.6. The particles inside and at grain boundaries consist predominantly of copper and iron (and of course of Al). Copper and iron could be found in almost all primary phase particles.

In the case of the AlLi alloy, certain inhomogeneities were found not only in Al, Cu, and Fe distributions but also in the Mg and Ag ones. EDX maps of the selected area of the AlLi sample are shown in Fig. 3.7. Again, the coarser particles consist predominantly of copper and iron, but some of them contain also Mg and Ag. Pure Ag is present in small spherical particles (diameter of tens of nanometers).

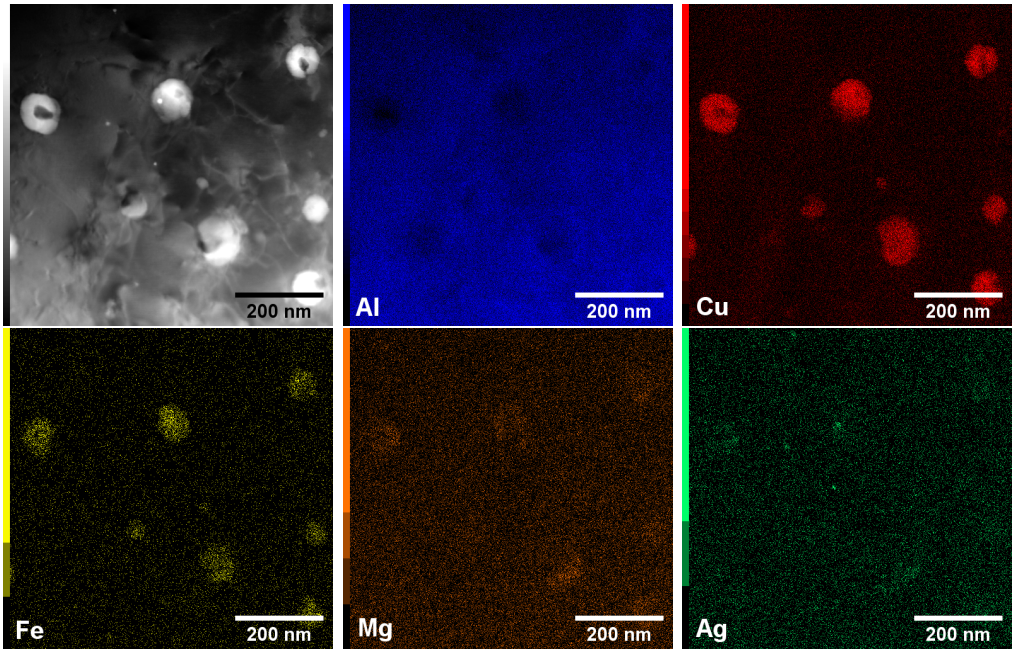

Fig. 3.7: STEM-UDF and EDX maps of the AlLi alloy.

3.3 Resistivity measurement

The measurement of electrical resistivity serves as an indicative measurement in which deviations from Matthiesen's rule indicate significant changes in the distribution of alloying elements inside the alloy.

Within the homogenization annealing process, the main goal is to dissolve coarse particles and to enrich the matrix by solutes.

The coarse particles are weak points in the material, because they serve as stress concentrators and preferential positions for the crack formation. Small, evenly distributed particles throughout the material, on the other hand, have a beneficial reinforcing effect.

In-situ resistivity measurements were performed for sample AlLi heated from 24 °C to 598 °C and sample AlLiSc from 33 °C to 600 °C. The measured resistance values were divided by the resistance at the initial temperature to obtain the relative resistivity evolution curve, see Fig. 3.8 and Fig. 3.9.

Figures 3.8 and 3.9 also show the resistance derivation curve (the derivative of resistance with respect to temperature, divided by the resistance at the initial temperature). This curve shows in more detail the rate of changes on the relative

resistivity curve. The inflection points of the resistivity curve are represented in the derivative curve by local maxima or minima. Minor oscillations on the derivative are the consequence of the numerical processing and insufficient data filtering.

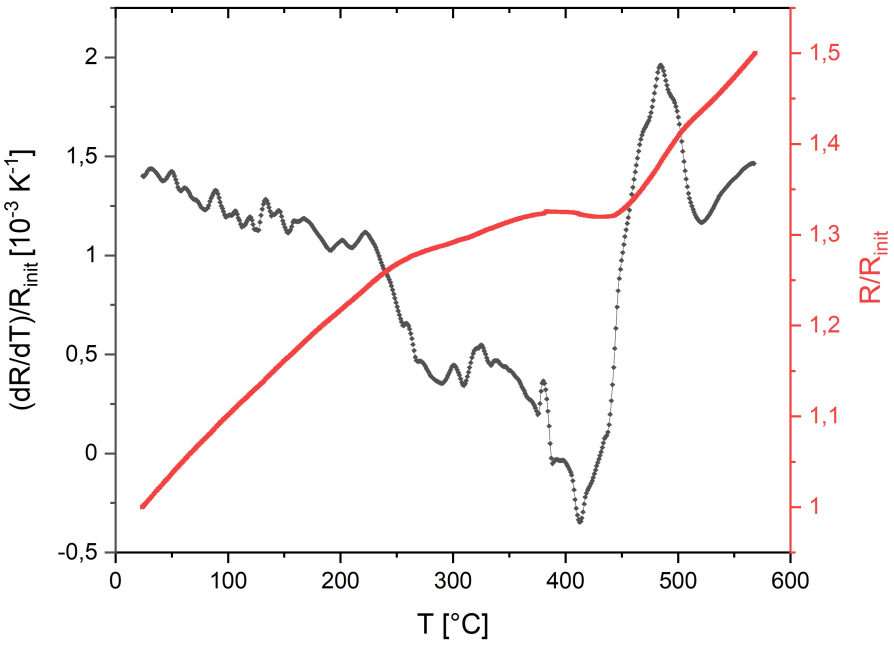

Fig. 3.8: AlLi relative resistivity curve (red) and resistivity derivative curve (black).

The relative resistivity curve for alloy AlLi grows almost with a constant rate up to 255 °C, followed by a lower growth rate. After reaching an indistinct local maximum at 384 °C, the resistance decreases slowly to a minimum at 432 °C. Afterwards, it grows relatively rapidly up to 500 °C, followed again by an increase with a similar rate as at the beginning of the experiment.

The rate of resistivity changes of both alloys coincides up to approximately 70 °C (see Fig. 3.10). After this temperature, the AlLiSc relative resistivity curve rises more slowly than the AlLi one up to 220 °C, from where it begins to increase sharply up to a maximum at around 305 °C. The maximum is followed by a slight decrease to the minimum at 324 °C. The curve rises again to the second maximum at 435 °C, decreases to the second minimum at 485 °C, and finally rises sharply, with a final inflex point at 537 °C.

In general, for aluminum alloys, the decrease in the resistivity rate is associated with the depletion of the solid solution, i.e., the precipitation of new particles. On the contrary, when the resistivity increases above the baseline, the matrix is enriched with solutes. The present particles are dissolved, both primary, formed during solidification of the melt, and secondary, formed by precipitation at lower temperatures.

In the AlLiSc alloy, the increase of the resistivity above 300 °C is suppressed by the formation and growth of Sc particles.

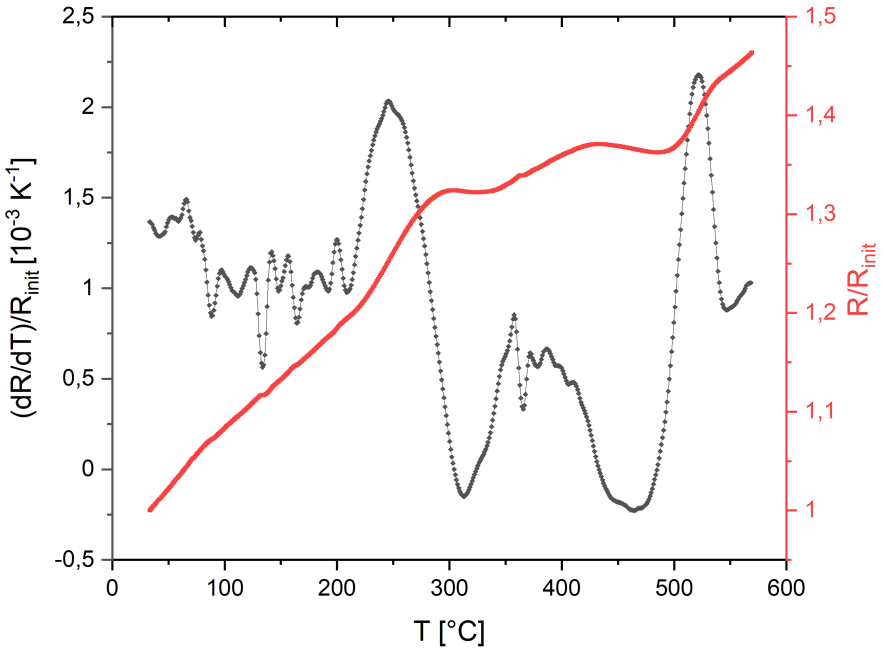

Fig. 3.9: AlLiSc relative resistivity curve (red) and resistivity derivation curve (black).

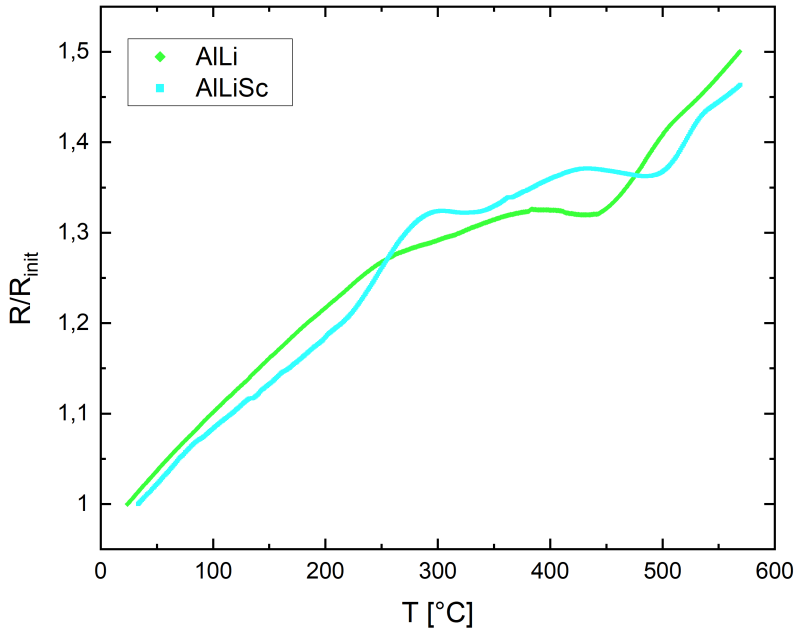

Fig. 3.10: Comparison of AlLi (green) and AlLiSc (blue) relative resistivity curve.

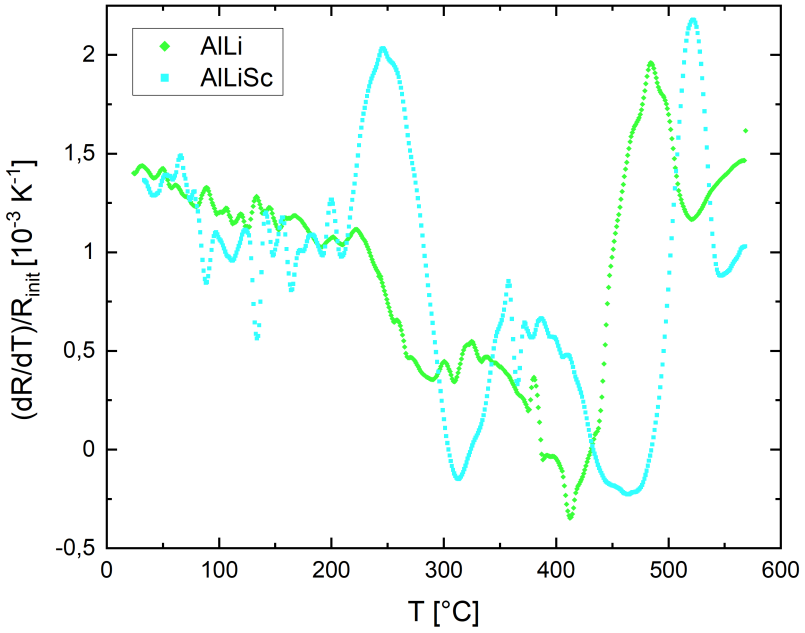

Fig. 3.11: Comparison of AlLi (green) and AlLiSc (blue) resistivity derivation curve.

At higher temperatures (above 400 °C), lithium can also evaporate in Al-Li-based alloys, resulting in a matrix purification and a decreased of the resistivity. The final process of reducing the resistivity of both alloys is therefore probably associated with a depletion of the material from lithium.

The main difference between AlLi and AlLiSc curve could be observed in the temperature range 220 °C - 350 °C (see Fig. 3.10 and Fig. 3.11).

3.4 STEM observation of in-situ heating

Observations of samples in TEM during in-situ heating could help to better understand and describe processes occuring during annealing. TEM samples of AlLi and AlLiSc material were placed in a holder that allowed direct heating of the sample inside the TEM (STEM) microscope.

We heated the specimens from 20 °C up to 540 °C increasing the temperature by 20 °C every 5 minutes. Stabilization of the new temperature usually took 1 to 2 minutes and the remaining time was used for the recording of images in bright field (BF) and upper dark field (UDF) contrasts. Recorded images show always the same place on the sample, at the same magnification.

3.4.1 AlLi alloy

In the case of the AlLi alloy, no visible changes were observed up to 200 °C, see Fig. 3.12a and Fig. 3.12b.

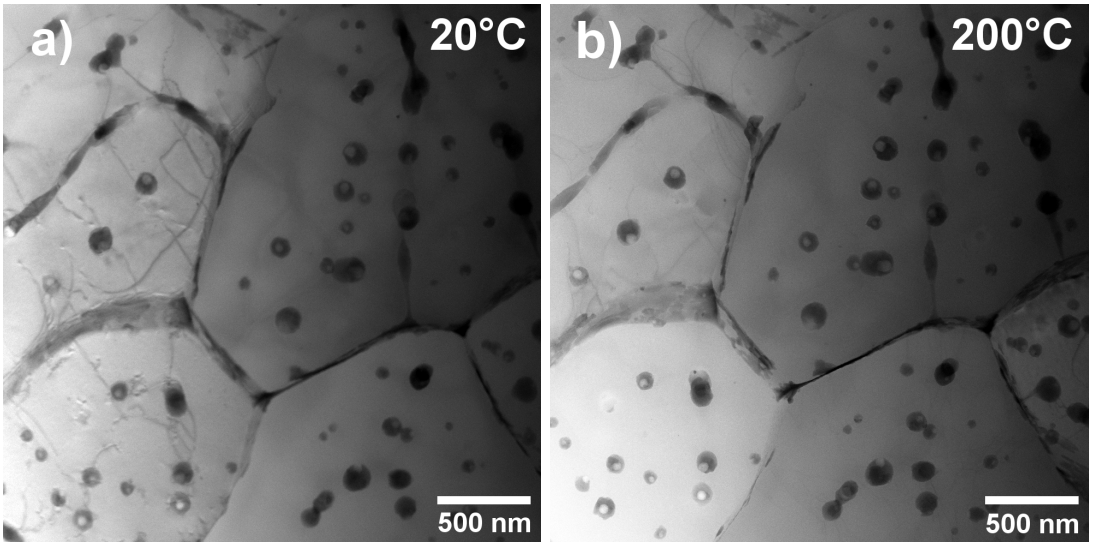

Fig. 3.12: STEM (BF) observations of AlLi sample during in-situ anenealing at room temperature (a) and at 200 °C (b).

At 220 °C, the formation of platelet-shaped particles occurs (probably T_1 phase). Also at 240 °C, thin needle-shaped particles begin to form (see Fig. 3.13a). More of these secondary particles forms, and they become coarser with increasing temperature (see Fig. 3.13b). At 340 °C, the particles partially dissolve (see Fig. 3.13c) and by reaching the temperature 400 °C, they are entirely dissolved.

The majority of primary particles, both inside the grains and those at grain boundaries, begin to grow already at 260 °C. However, at 380 °C, both coarsening and dissolution of primary particles begin, but some particles at grain boundaries do not dissolve but rather start to form clusters (see Fig. 3.13d).

A continuous growth, coarsening, and dissolution of particles occurs between 420 - 540 °C, and finally, only several particles remain at grain boundaries and at triple points at 540 °C. The evolution of primary particles is shown in the sequence of images in Fig. 3.14.

3.4.2 AlLiSc alloy

No visible modifications of the microstructure were observed in the sample up to 200 °C (Fig. 3.15).

Between 220 and 260 °C, needle-shaped and platelet-shaped secondary particles begin to form (marked by a circle in Fig. 3.16a) similarly as in the AlLi alloy. Small, spherical, homogeneously distributed particles start to form at 320 °C and the entire volume of the sample is already evenly sown with these small particles at 380 °C (see Fig. 3.16d). They are present in the sample until the end of the measurement and the only change at higher temperatures is their partial dissolution and coarsening.

The transformation of primary phase particles is very similar to the one observed in the AlLi alloy. Partial coarsening of both, grain boundary particles and particles inside grains occurs between 260 - 380 °C (see Fig. 3.16). A continuous growth of several newly formed grain boundary particles, gradual coarsening and

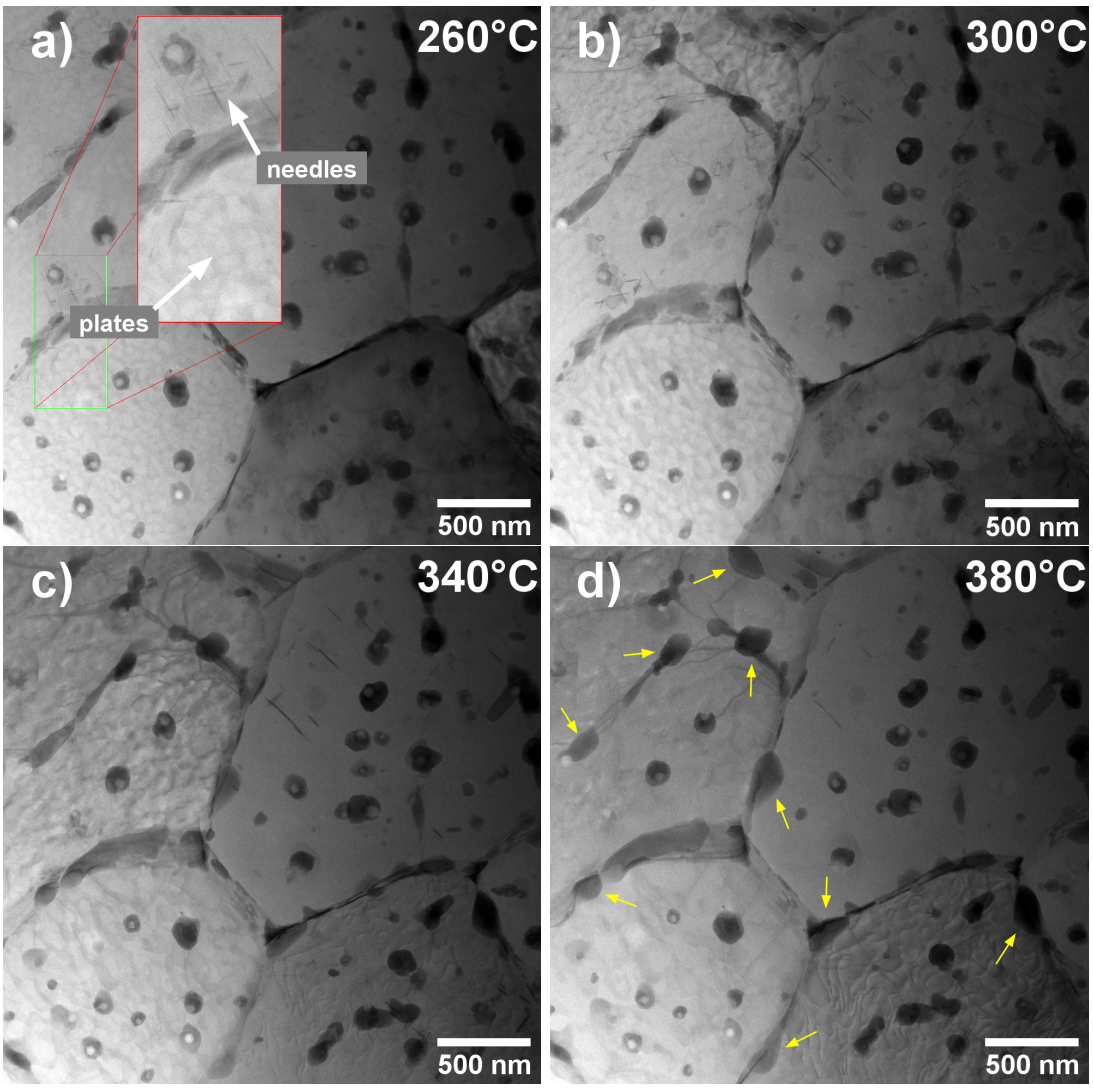

Fig. 3.13: STEM (BF) observations of secondary particles formed during in-situ annealing of AlLi specimen. Some of needle-shaped and platelet-shaped particles are zoomed in (a). Yellow arrows in (d) are pointing at coarsened primary particles (compare with the same places in (a) or Fig. 3.12).

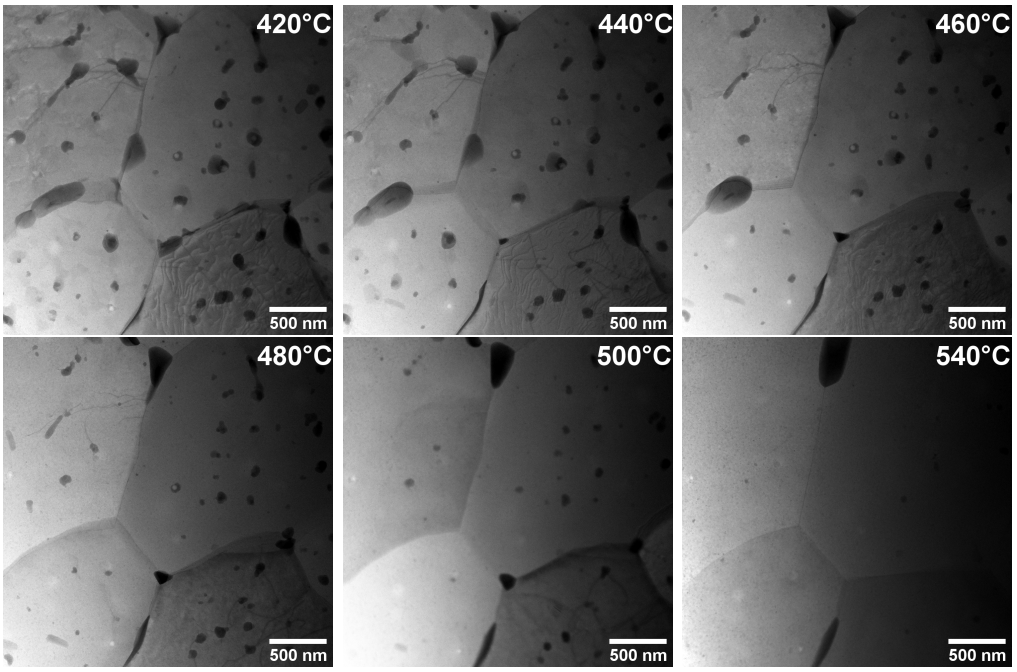

Fig. 3.14: STEM (BF) observations during in-situ annealing of the AlLi alloy between 420 - 540 °C.

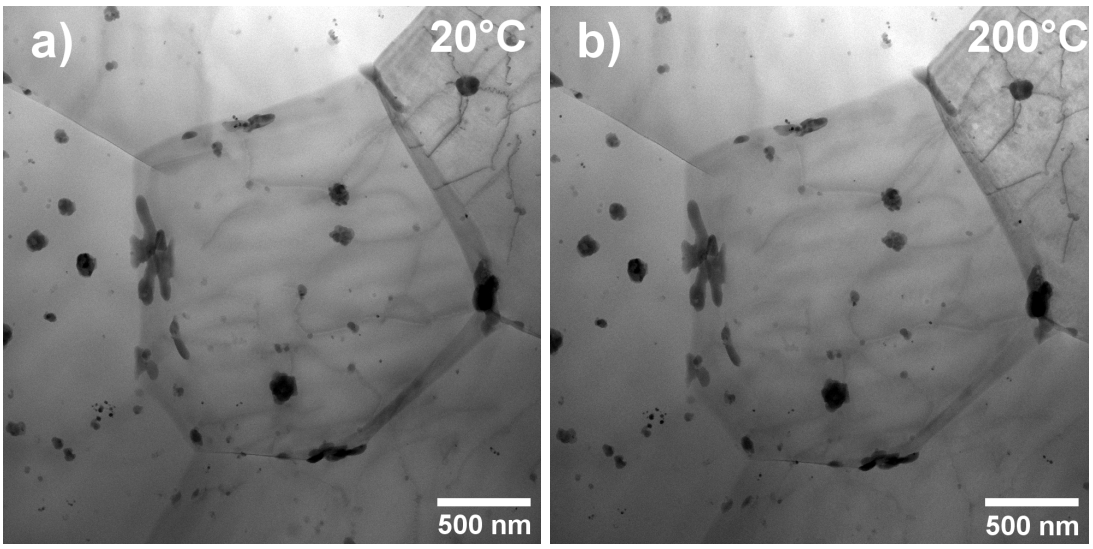

Fig. 3.15: STEM (BF) observation of AlLiSc sample during in-situ annealing at room temperature (a) and at 200 °C (b).

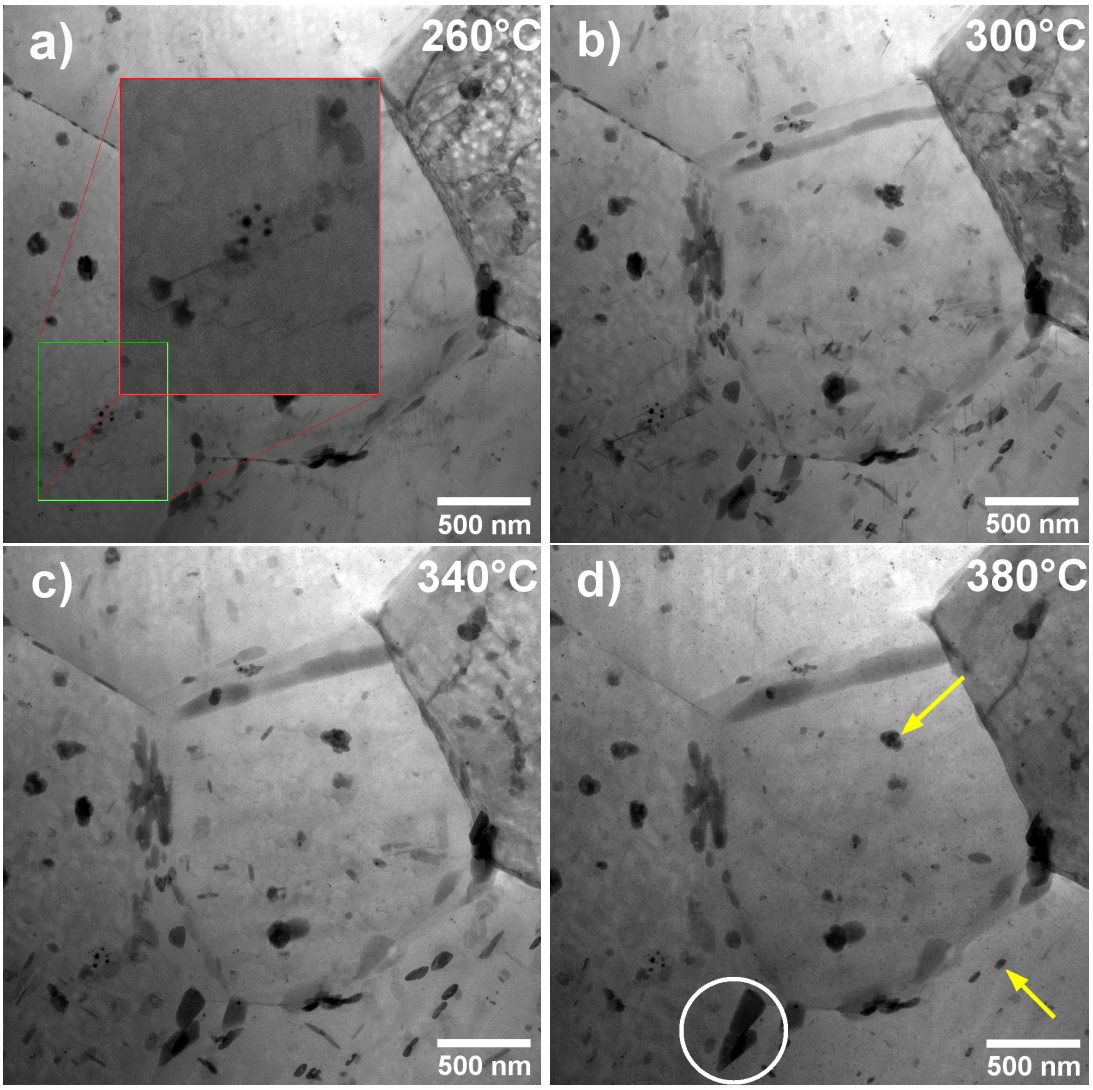

Fig. 3.16: STEM (BF) observation of secondary and primary particle evolution in AlLiSc sample during in-situ annealing in the temperature range 260 - 380 °C. Zoomed inset in (a) shows some of newly-formed needle-shaped particles. The platelet particles are visible over almost the entire surface of the sample. The arrows in (d) indicate dissolving particles, the circle indicates coarse particles at the grain boundary - compare with (a) - (c).

entire dissolution of remaining ones could be observed between 420 - 540 °C (see Fig. 3.17).

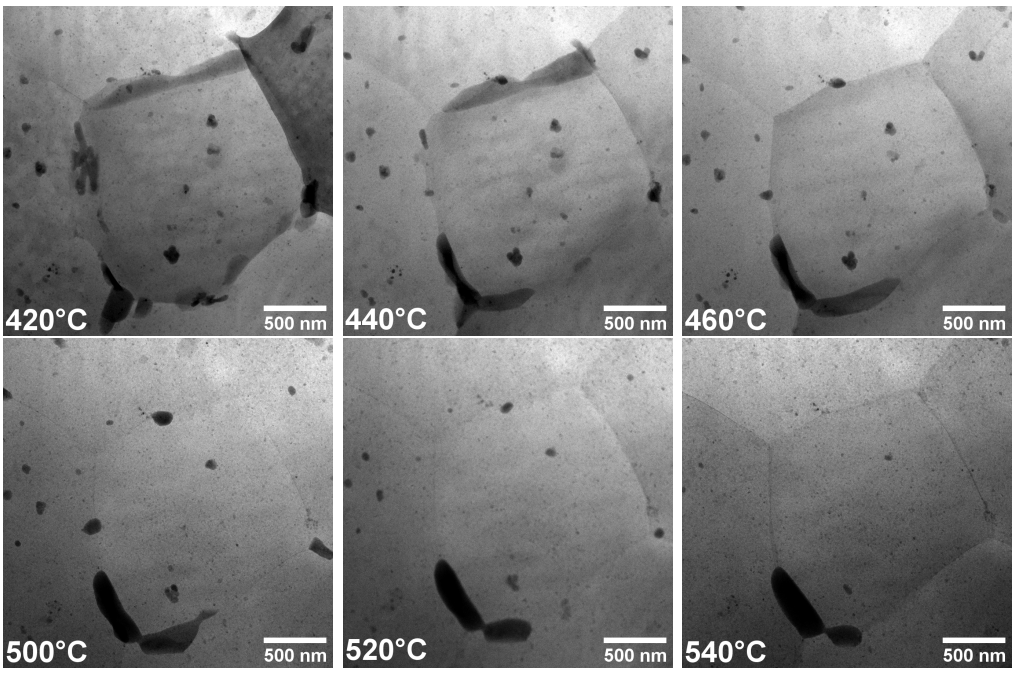

Fig. 3.17: STEM observation of AlLiSc sample during in-situ anenealing.

3.5 Final state

The study of the annealed (final) state of AlLi and AlLiSc alloys consisted of imaging the altered microstructure by STEM, performing EDX analyses of selected places of the samples, and subsequent analyses of diffraction patterns for the crystallographic phase determination.

Figure 3.18 shows a comparison of the microstructure of both alloys after they have been annealed in-situ in TEM up to 540 °C and fast cooled (in TEM) to the room temperature during 1 min.

Grains in both alloys are not modified by annealing. In the case of AlLi alloy, the grains are generally smaller; however, more statistical analyses are necessary to support this conclusion. The grain size is around 4 μm in AlLi alloy and about 7 μm in AlLiSc alloy.

It can be seen that primary particles distributed initially at grain boundaries and grain interiors transformed into new grain boundary ones. The grain interior does not contain coarse particles, which were observed in the initial state of the alloy. At larger magnification it is possible to find smaller particles homogeneously distributed within the grains. They are Zr-containing ones in the AlLi alloy and (Zr+Sc)-containing ones in the AlLiSc alloy.

The second step in the examination of the annealed state of the alloys was EDX analysis. The series of images in Fig. 3.19 and Fig. 3.20 shows EDX maps of main detected elements in selected areas of AlLi and AlLiSc alloys.

In contrast to the initial state, it is possible to find coarse zirconium particles in both alloys. Most probably, they are particles of the equilibrium phase Al_3Zr.

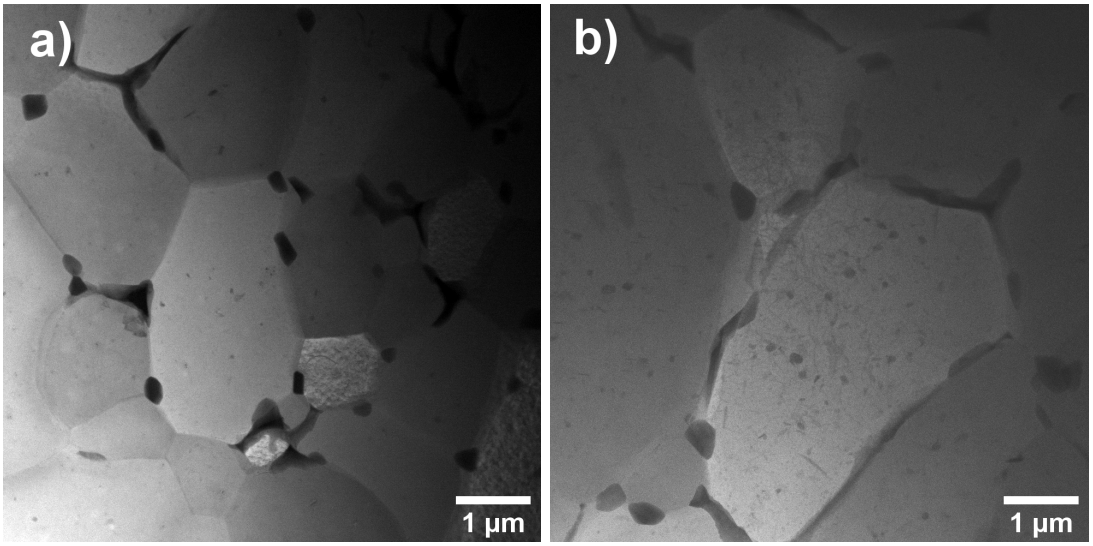

Fig. 3.18: STEM (BF) images of AlLi (a) and AlLiSc (b) alloy microstructure after in-situ annealed up to 540 °C and fast cooled down to RT.

Moreover, the second feature is a clear separation of Cu-containing particles from Fe ones indicating a formation of new phases in the final state. Sc is rather under the resolution limit, and forms a homogeneous background on maps and therefore is not included in Fig. 3.19 and Fig. 3.20.

In an attempt to characterize the crystallography of final particles, SAED analyses were performed on Cu and Fe-containing particles. Selected diffraction patterns together with the corresponding TEM images are shown in Fig. 3.21 and Fig. 3.22 (for the AlLi alloy), and in Fig. 3.23 and Fig. 3.24 (for the AlLiSc alloy).

After the identification of a periodic figure in the diffraction pattern, the distances of diffraction spots using the ImageJ software were measured (distances between several spots were measured in order to achieve better accuracy). The inverted values of measured distances define values of interplanar distances of diffracting planes. By comparing SAED findings with Pearson's Crystal Database and respecting EDX results, it is possible to partially identify the crystallographic structures of the final phases.

The longest interplanar distances calculated for Cu-rich particles are (in nm) 0.44, 0.43, 0.31, 0.28, 0.25, 0.24, 0.22, and for Fe-rich particles are (in nm) 0.64 and 0.49. They are with agreement with R-phase Al_5CuLi_3 (Im-3; $a = b = c = 1.39056$ nm; $\alpha = \beta = \gamma = 90°$ [24]) in the case of Cu-rich particles and with $Al_{13}Fe_4$ phase (C12/m1; $a = 1.5495$ nm, $b = 0.8089$ nm, $c = 1.2485$ nm; $\alpha = 90°$, $\beta = 107.7°$, $\gamma = 90°$ [25]) in the case of Fe-rich ones. However, for a full identification a complex analysis based on a simulation of diffraction patterns is necessary.

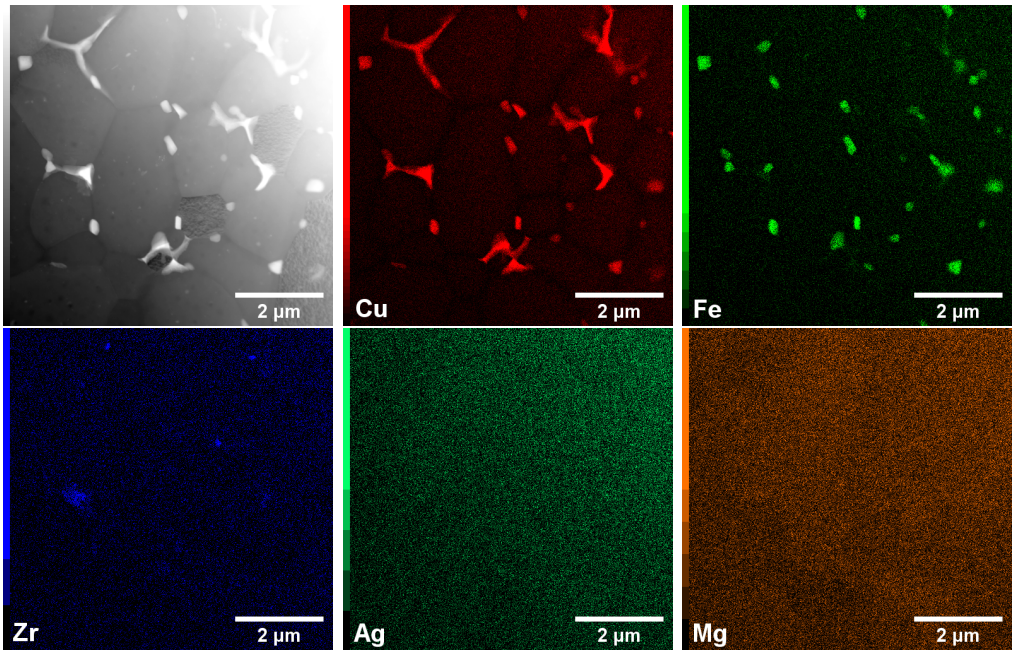

Fig. 3.19: STEM-UDF and EDX maps of the AlLi sample after in-situ TEM heating up to 540 °C.

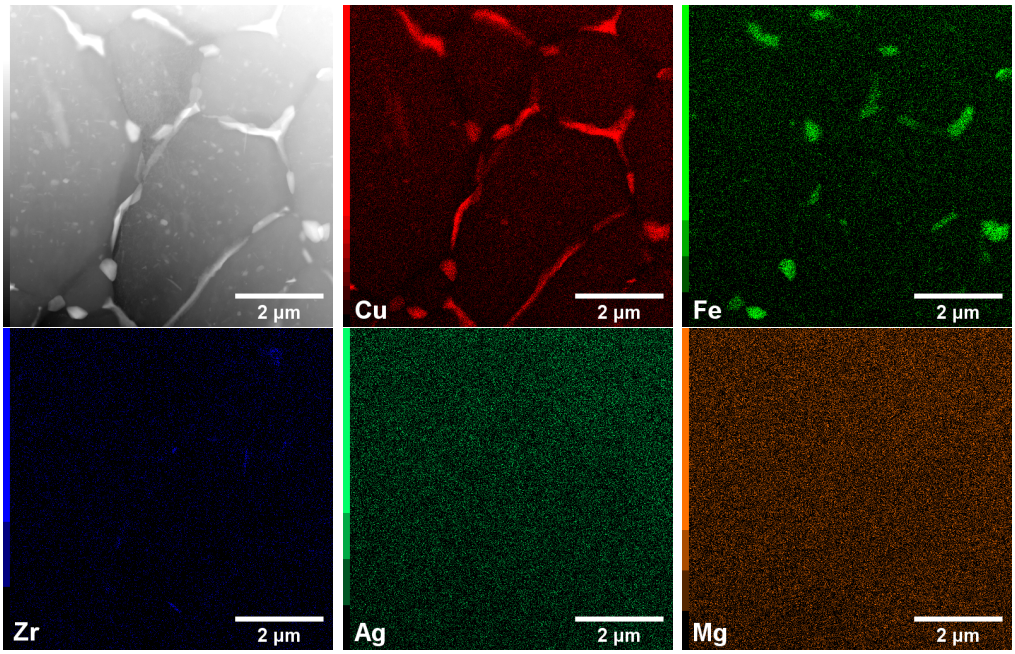

Fig. 3.20: STEM-UDF and EDX maps of the AlLiSc sample after in-situ TEM heating up to 540 °C.

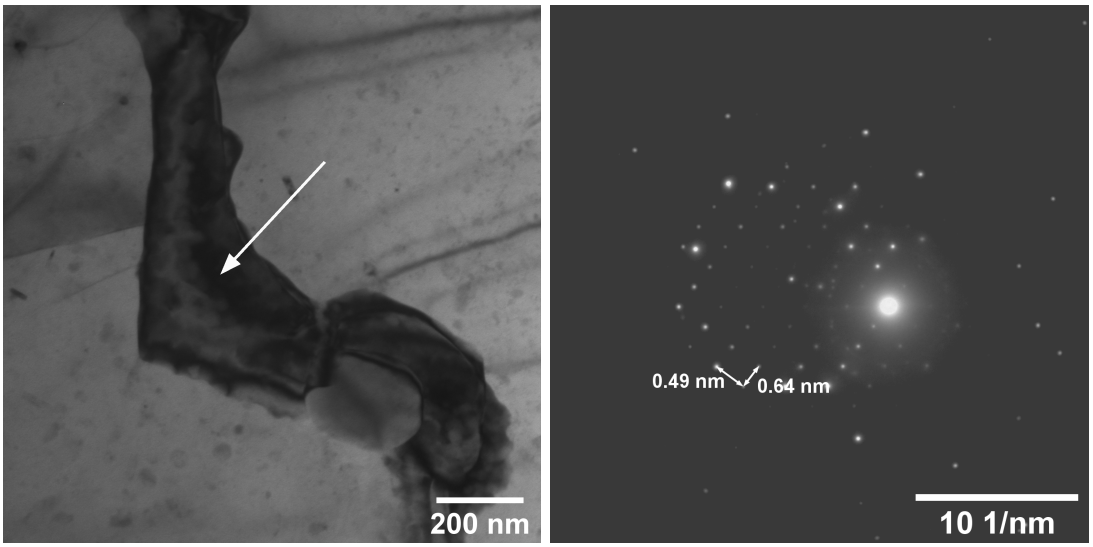

Fig. 3.21: Diffraction pattern of copper containing particle inside the AlLi specimen in-situ TEM heated up to 540 °C.

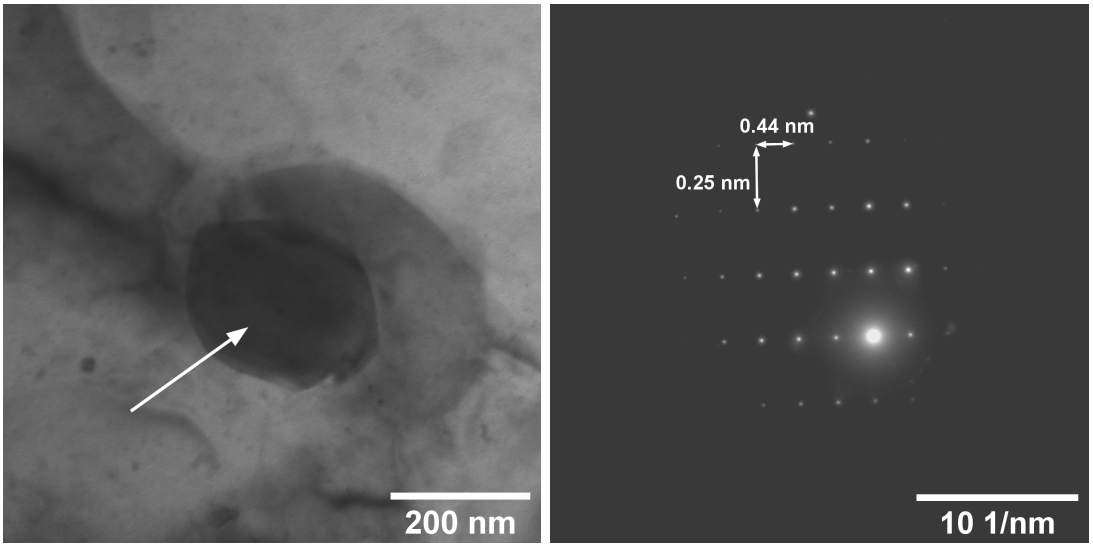

Fig. 3.22: Diffraction pattern of ferrous particle inside the AlLi specimen in-situ TEM heated up to 540 °C.

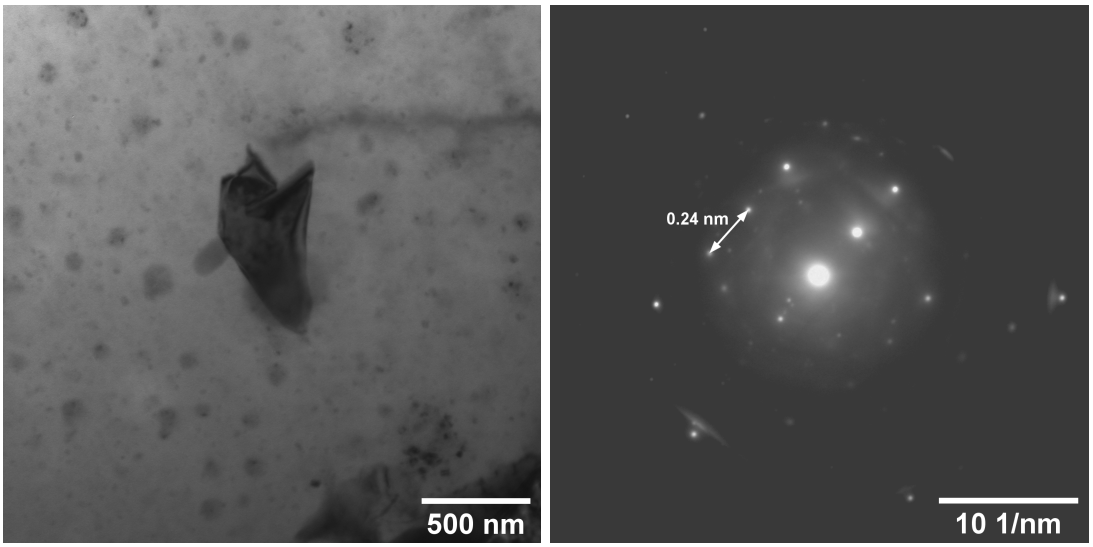

Fig. 3.23: Diffraction pattern of a selected particle in AlLiSc specimen in-situ TEM heated up to 540 °C.

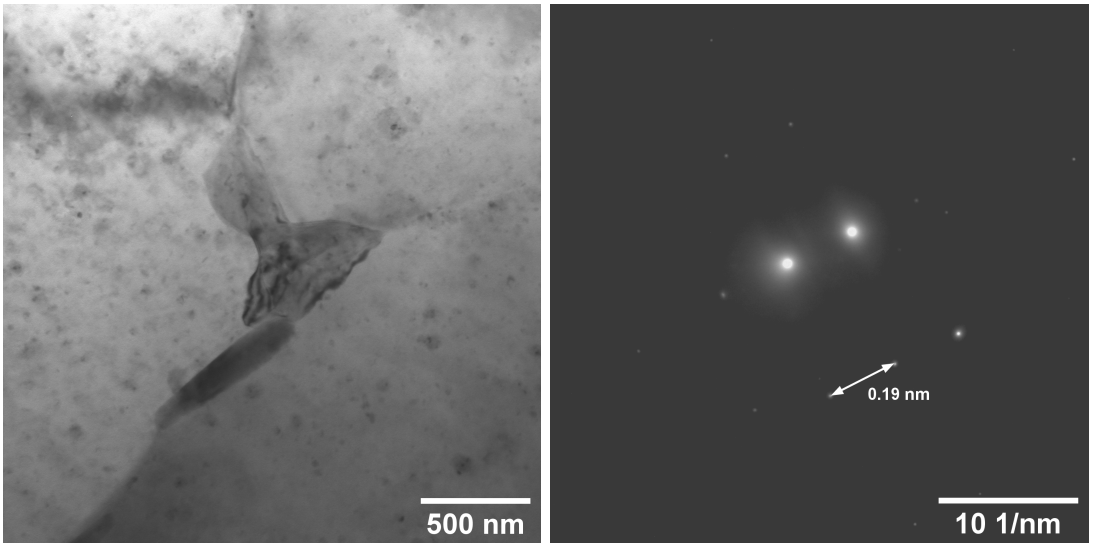

Fig. 3.24: Diffraction pattern of a selected particle in AlLiSc specimen in-situ TEM heated up to 540 °C.

4. Discussion

In-situ TEM (STEM) observations could help to interpret the shape of observed resistivity changes. As can be seen, up to 220 °C, the resistivity curve rises evenly (as assumed by Matthiesen's rule), which corresponds well with STEM observations, since no changes of the microstructure have been detected in this temperature interval.

Above 220 °C, emerging platelet-shaped particles appear. These particles further grow up to about 320 °C. This process is further combined with a formation and coarsening of needle-shaped particles between 240 and 300 °C. Moreover, a slight coarsening of particles of primary phases could be observed. All these phenomena are related to the depletion of the sample matrix, thus resulting in a complicated slowing of the resistivity growth.

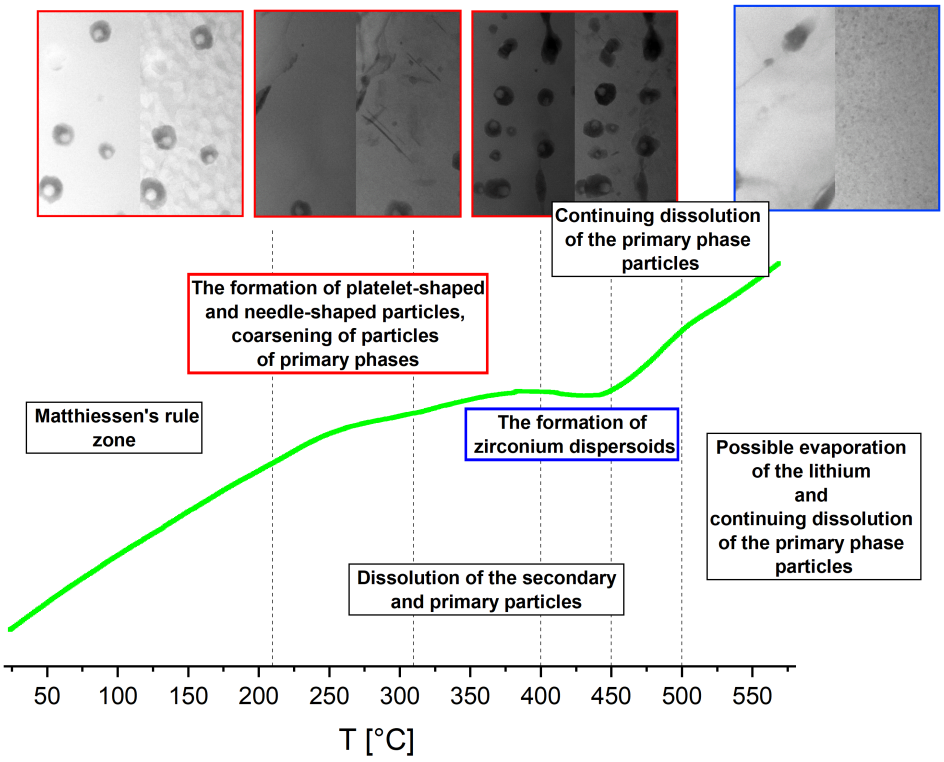

Fig. 4.1: AlLi alloy: correspondence between STEM and resistivity experiments.

Above 300 °C, the growth of the curve is again slightly accelerated, which we associate with the dissolution of secondary and primary particles (inside and at the grain boundaries) and re-enrichment of the matrix. This dissolution is observed in a microscope until the end of the measurement. However, the resistivity curve still shows one deviation from the Matthiessen's rule - a decrease in resistivity, in the range of 400 °C to 470 °C. Upon closer examination of the STEM images, dispersoids similar to scandium particles observed in the AlLiSc alloy were detected. These homogeneously distributed dispersoids are the particles of non-equilibrium Al_3Zr phase and the decrease in resistivity is attributed to their formation.

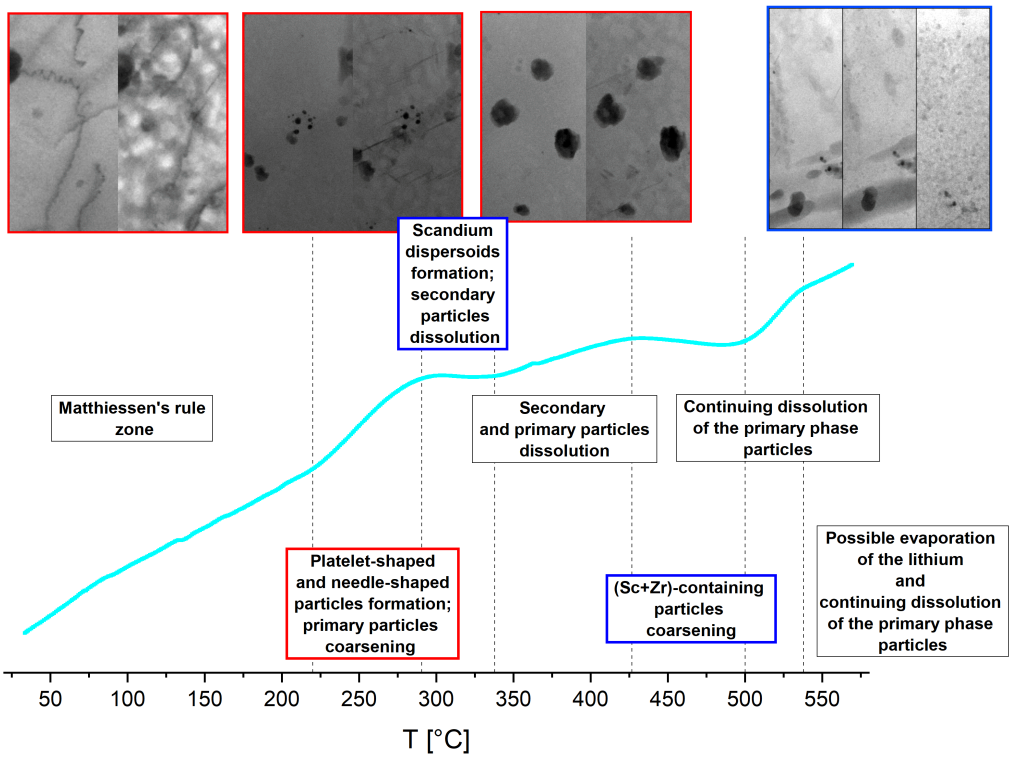

Fig. 4.2: AlLiSc alloy: correspondence between STEM and resistivity experiments.

Similar examination of the resistivity curve was done also for the AlLiSc alloy. Up to 220 °C, the evenly increasing trend of the resistivity curve agrees with STEM records, with no microstructural change in the sample.

However, the graph area in the temperature range from 220 °C to 280 °C is slightly inconsistent with the observations. As in the AlLi alloy, platelet-shaped particles begin to form at a temperature of 220 °C (needle-shaped particles also at a higher temperature). The formation of these particles in conjunction with the coarsening of the primary phase particles does not explain the steeper growth of the resistivity curve; on the contrary, we would expect a slowdown in the resistivity growth as the one observed in the AlLi alloy. We have not yet been able to clarify this discrepancy. From 320 °C a dissolution of secondary particles begins, but Sc-containing particles precipitate simultaneously. The interplay of these two phenomena creates a plateau or even a decrease in the resistivity curve. At 340 °C, the dissolution effect of the primary particles prevails, as a result of which the resistivity curve rises again. At 430 °C, nothing unusual was found in the STEM images, but the resistivity curve begins to drop again. We explain this decrease by a precipitation of zirconium-containing particles or a formation of complex particles of the Al_3Zr phase on the surface of already existing scandium (Al_3Sc) particles. Above 500 °C, the curve only grows again with a slight deceleration at 530 °C, which we again explain by a depletion of the aluminum matrix from lithium.

Examination of EDX maps of samples of both alloys in the original state and the state after annealing at 540 °C and rapid cooling to room temperature shows a change in the composition of the main phases in both samples. While in the

original state, all the observed phases contained both Cu and Fe (most probably the Al_7Cu_2Fe phase known from the literature [8]), in the annealed state, the Fe and Cu-containing phases are generally found separately (see Fig. 4.3 and Fig. 4.4) indicating that the initial Al_7Cu_2Fe phase is substituted by $Al_{13}Fe_4$ and Al_5CuLi_3 phases. Another difference is the presence of Zr-containing phases in the final state (see Fig 3.19 and Fig. 3.20). They could form during annealing but their relatively large size indicates, that most probably they were present in the material already in the initial state and they were not found during the EDX analysis due to an insufficient statistics.

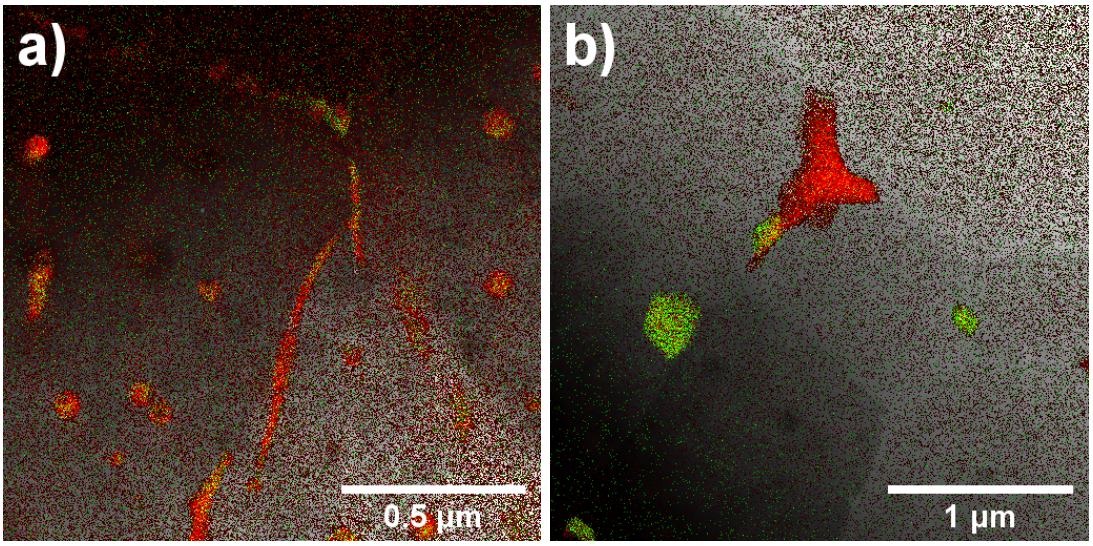

Fig. 4.3: An overlay of Cu and Fe EDX map on STEM-UDF in the initial state (a) and in the annealed state (b) of the AlLi alloy.

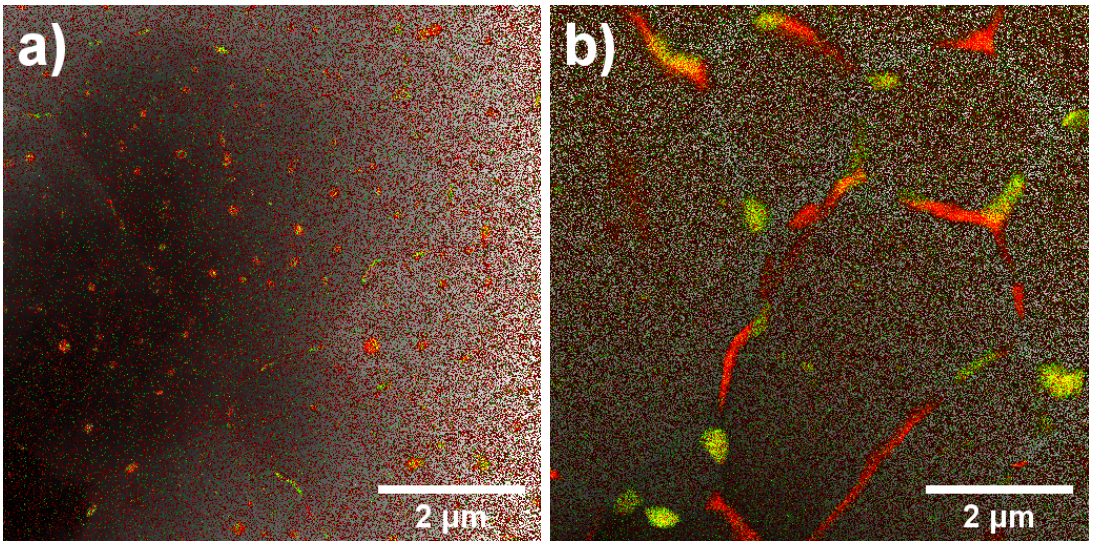

Fig. 4.4: An overlay of Cu and Fe EDX map on STEM-UDF in the initial state (a) and in the annealed state (b) of the AlLiSc alloy.

Conclusions

To obtain the basic information about the microstructure of AlLi and AlLiSc alloys prepared by RSD melt-spinning method, LOM, STEM, and EDX observations of the initial state were performed. To determine the temperature intervals at which phase transformations occur, resistometric in-situ measurements for both alloys for temperatures between 25 °C and $\sim$ 600 °C were performed. The stability of RSD ribbons was studied during in-situ TEM heating (from room temperature up to 540 °C). Subsequently TEM (STEM) observations and EDX analyses of annealed states were performed. Finally, diffraction patterns were captured to identify the phases formed in the annealed state of samples.

The microstructure of both alloys consists of fine grains with coarse primary particles formed predominantly at grain boundaries. During the in-situ annealing, the formation of secondary platelet-shaped and needle-shaped particles (probably phases T_1 and S'), coarsening of primary phase particles, formation of Sc- and Zr-containing dispersoids and subsequent dissolution of majority of phases were observed gradually.

Large particles inside grains were mostly absent in the microstructure of both annealed alloys. The majority of large particles remaining in the annealed materials was situated at grain boundaries. In addition, non-equilibrium Al_3Zr (in the case of AlLi alloy) and $Al_3(Sc, Zr)$ particles (in the case of AlLiSc alloy) tens of nanometers large, evenly distributed in the grains, were formed.

STEM in-situ observations matched with resistometric in-situ measurements with one exception - a sharp increase in resistivity for AlLiSc alloys in the range of 220 - 280 °C. The origin of this effect has not been explained yet.

EDX analyzes determined the chemical composition of the major phases in the initial and annealed state. The particles in the initial state consisted mainly of Al-Cu-Fe (most probably Al_7Cu_2Fe phase), while in the annealed state, Cu and Fe appeared separately in different particles. Diffraction patterns indicate that R-phase (Al_5CuLi_3) is present in copper-rich particles of the samples along with a typical iron phase $Al_{13}Fe_4$ in iron-rich particles.

Bibliography

[1] P. Haasen. *Physical Metallurgy*. Cambridge University Press, 1978.

[2] R. J. Rioja and J. Liu. The Evolution of Al-Li Base Products for Aerospace and Space Applications. *Metallurgical and Materials Transactions A*, 43:3325–37, 2012.

[3] E. A. Starke and J. T. Staley. Application of modern aluminum alloys to aircraft. *Progress in Aerospace Sciences*, 32:131–172, 1996.

[4] T. S. Srivatsan and E. J. Lavernia. The presence and consequences of precipitatefree zones in an aluminium-copper-lithium alloy. *Journal of Materials Science*, 26:940–950, 1991.

[5] V. Raghavan. Al-Cu-Li (Aluminum-Copper-Lithium). *Journal of Phase Equilibria and Diffusion*, 31:288–290, 2010.

[6] H. M. Flower and P. J. Gregson. Solid state phase transformations in aluminium alloys containing lithium. *Materials Science and Technology*, 3:81–90, 1987.

[7] W. Yang, L. Hongyu, M. Xiaochun, W. Ruizhi, S. Jianfeng, H. Legan, Z. Jinghuai, L. Xinlin, and Z. Milin. Effects of Sc and Zr on microstructure and properties of 1420 aluminum alloy. *Materials Characterization*, 154:241–247, 2019.

[8] K. B. Kalmykov, N. L. Zvereva, S. F. Dunaev, N. V. Kazennov, E. V. Tat'yanin, G. V. Semernin, N. E. Dmitrieva, and Yu. V. Balykova. Phase equilibria in the Al-Cu-Fe system at a temperature of 853 K in the aluminum enriched region. *Moscow University Chemistry Bulletin*, 64:99–103, 2009.

[9] Ch. Fuller, J. Murray, and D. Seidman. Temporal evolution of the nanostructure of Al(Sc,Zr) alloys: Part I - Chemical compositions of Al-3(Sc1-xZrx) precipitatesy. *Acta Materialia*, 53:5401–5413, 12 2005.

[10] P. Duwez, R. H. Willens, and W. Klement Jr. Continuous Series of Metastable Solid Solutions in Silver-Copper Alloys. *Journal of Applied Physics*, 31:1136–37, 1960.

[11] M. Sherif El-Eskandarany. In M. Sherif El-Eskandarany, editor, *Mechanical Alloying*, pages 1–11. William Andrew Publishing, third edition, 2020.

[12] M. Swaroopa, L. Venu Gopal, T. Kishen Kumar Reddy, and B. Majumdar. Effect of Crucible Parameters on Planar Flow Melt Spinning Process. *Transactions of the Indian Institute of Metals*, 68:1125–29, 2015.

[13] E. Abbe. Beiträge zur Theorie des Mikroskops und der mikroskopischen Wahrnehmung. *M. Schultze's Archiv für mikroskopische Anatomie*, 9:413–468, 1873.

[14] Y. Leng. *Materials characterization: Introduction to microscopic and spectroscopic methods*. J. Wiley, 2008.

[15] NobelPrize.org. J.J. Thomson – Biographical. `https://www.nobelprize.org/prizes/physics/1906/thomson/biographical/`, May 2021.

[16] P. Weinberger. Revisiting Louis de Broglie's famous 1924 paper in the Philosophical Magazine. *Philosophical Magazine Letters*, 86:405–410, 2006.

[17] E. Ruska and M. Knoll. The Electron Microscope. *Z. Physics*, 78:318–339, 1932.

[18] E. Ruska. Advances in Building and Performance of the Magnetic Electron Microscope. *Z. Physics*, 78:580–602, 1934.

[19] H. Nukala. Quantitative Thickness Mapping In High-angle Annular Darkfield (HAADF) Scanning Transmission Electron Microscopy (STEM). *Electronic Theses and Dissertations*, pages 2004–2019, 3670, 2008.

[20] P. Rez, T. Larsen, and M. Elbaum. Exploring the theoretical basis and limitations of cryo - STEM tomography for thick biological specimens. *Journal of Structural Biology*, 196:466–478, 2016.

[21] U. Motohiro, W. Takahiro, and S. Tomoko. Applications of X-ray fluorescence analysis (XRF) to dental and medical specimens. *Japanese Dental Science Review*, 01 2014.

[22] Ch. Kittel. *Introduction to solid state physics*. J. Wiley, 1956.

[23] Charles University. In-situ resistivity measurement. `https://www.mff.cuni.cz/en/kfm/experimental-facilities/electrical-resistivity`, May 2021.

[24] M. Audier, J. Pannetier, M. Leblanc, C. Janot, J. Lang, and B. Dubost. An approach to the structure of quasicrystals: A single crystal X-ray and neutron diffraction study of the R-Al5CuLi3 phase. *Physica B: Condensed Matter*, 153:136–142, 1988.

[25] S. Kazumasa, O. Tatsuo, and H. Kenji. The Crystalline Structure of O-AlFePd. *Electronic Theses and Dissertations*, 53:1357–1362, 2012.

List of Figures

1.1 Free energy and common tangent construction [1]. 4
1.2 Derivation of a binary phase diagram from free energy curves for solid phase α and melt phase L [1]. 4
1.3 Derivation of an eutectic binary phase diagram from free energy evolution at different temperatures [1]. 5
1.4 Derivation of peritectic binary phase diagram from free energy evolution at different temperatures [1]. 5
1.5 Al-rich region of the computed Al-Cu-Li ternary phase diagram at 500°C [5]. 7
1.6 Al-rich corner of the Al-Cu-Mg ternary phase diagram at 200°C [6]. 7
1.7 Al-rich corner of isothermal section of the computed Al-Sc-Zr ternary phase diagram [9]. 7
1.8 Schematics of the melt-spinning process (the RSP used in the thesis for the sample preparation) [12]. 8
1.9 An example of an alloy prepared by melt-spinning. 8

2.1 Imaging (a) and diffraction (b) mode of the transmission electron microscope [19]. 11
2.2 CTEM and STEM scheme comparison 11
2.3 Scheme for characteristic X-ray notation [21]. 12

3.1 Sections through the AlLi RSD ribbon. 15
3.2 Sections through the AlLiSc RSD ribbon. 16
3.3 STEM overview of the AlLiSc alloy in BF (a) and UDF (b) contrasts. 17
3.4 Detailed TEM images of the AlLi alloy. 17
3.5 STEM detailed images of the AlLiSc alloy. 18
3.6 STEM-UDF and EDX maps of the AlLiSc alloy (selected detail from Fig. 3.3). 18
3.7 STEM-UDF and EDX maps of the AlLi alloy. 19
3.8 AlLi relative resistivity curve (red) and resistivity derivative curve (black). 20
3.9 AlLiSc relative resistivity curve (red) and resistivity derivation curve (black). 21
3.10 Comparison of AlLi (green) and AlLiSc (blue) relative resistivity curve. 21
3.11 Comparison of AlLi (green) and AlLiSc (blue) resistivity derivation curve. 22
3.12 STEM (BF) observations of AlLi sample during in-situ anenealing at room temperature (a) and at 200 °C (b). 23
3.13 STEM (BF) observations of secondary particles formed during in-situ annealing of AlLi specimen. Some of needle-shaped and platelet-shaped particles are zoomed in (a). Yellow arrows in (d) are pointing at coarsened primary particles (compare with the same places in (a) or Fig. 3.12). 24

3.14 STEM (BF) observations during in-situ annealing of the AlLi alloy between 420 - 540 °C. 25
3.15 STEM (BF) observation of AlLiSc sample during in-situ annealing at room temperature (a) and at 200 °C (b). 25
3.16 STEM (BF) observation of secondary and primary particle evolution in AlLiSc sample during in-situ annealing in the temperature range 260 - 380 °C. Zoomed inset in (a) shows some of newly-formed needle-shaped particles. The platelet particles are visible over almost the entire surface of the sample. The arrows in (d) indicate dissolving particles, the circle indicates coarse particles at the grain boundary - compare with (a) - (c). 26
3.17 STEM observation of AlLiSc sample during in-situ anenealing. . . 27
3.18 STEM (BF) images of AlLi (a) and AlLiSc (b) alloy microstructure after in-situ annealed up to 540 °C and fast cooled down to RT. . 28
3.19 STEM-UDF and EDX maps of the AlLi sample after in-situ TEM heating up to 540 °C. 29
3.20 STEM-UDF and EDX maps of the AlLiSc sample after in-situ TEM heating up to 540 °C. 29
3.21 Diffraction pattern of copper containing particle inside the AlLi specimen in-situ TEM heated up to 540 °C. 30
3.22 Diffraction pattern of ferrous particle inside the AlLi specimen in-situ TEM heated up to 540 °C. 30
3.23 Diffraction pattern of a selected particle in AlLiSc specimen in-situ TEM heated up to 540 °C. 31
3.24 Diffraction pattern of a selected particle in AlLiSc specimen in-situ TEM heated up to 540 °C. 31

4.1 AlLi alloy: correspondence between STEM and resistivity experiments. 32
4.2 AlLiSc alloy: correspondence between STEM and resistivity experiments. 33
4.3 An overlay of Cu and Fe EDX map on STEM-UDF in the initial state (a) and in the annealed state (b) of the AlLi alloy. 34
4.4 An overlay of Cu and Fe EDX map on STEM-UDF in the initial state (a) and in the annealed state (b) of the AlLiSc alloy. 34

List of Tables

2.1 Chemical composition of the master aluminum alloy V242 9
2.2 Chemical composition of the master aluminum alloy V243 9

List of Abbreviations

RSP	Rapid solidification processing
RSD	Rapid solidification
wt.%	Weight percent
TEM	Transmission electron microscope
SEM	Scanning electron microscopy
STEM	Scanning transmission electron microscope
CTEM	Conventional transmission electron microscope
BF	Bright field
DF	Dark field
UDF	Upper dark field
HRTEM	High resolution TEM
LOM	Light optical microscopy
CCD	Charged Coupled Device
SiC	Silicon Carbide
BN	Boron-nitride
EDX	Energy-Dispersive X-ray (spectroscopy)
a, b, c α, β, γ	Lattice parameters